

CanadaFireSat: Toward high-resolution wildfire forecasting with multiple modalities

Hugo Porta^{a,*}, Emanuele Dalsasso^a, Jessica L. McCarty^b, Devis Tuia^a

^a*EPFL, Route des Ronquos 86, Sion, 1950, Wallis, Switzerland*

^b*NASA Ames Research Center, Earth Science Division,, Moffett Field, California, 94035, USA*

Abstract

Canada experienced in 2023 one of the most severe wildfire seasons in recent history, causing damage across ecosystems, destroying communities, and emitting large quantities of CO₂. This extreme wildfire season is symptomatic of a climate-change-induced increase in the length and severity of the fire season that affects the boreal ecosystem. Therefore, it is critical to empower wildfire management in boreal communities with better mitigation solutions. Wildfire probability maps represent an important tool for understanding the likelihood of wildfire occurrence and the potential severity of future wildfires. The massive increase in the availability of Earth observation data has enabled the development of deep learning-based wildfire forecasting models, aiming at providing precise wildfire probability maps at different spatial and temporal scales. A main limitation of such methods is their reliance on coarse-resolution environmental drivers and satellite products, leading to wildfire occurrence prediction of reduced resolution, typically around $\sim 0.1^\circ$. This paper presents a benchmark dataset: CanadaFireSat, and baseline methods for high-resolution: 100 m wildfire forecasting across Canada, leveraging multi-modal data from high-resolution multi-spectral satellite images (Sentinel-2 L1C), mid-resolution satellite products (MODIS), and environmental factors (ERA5 reanalysis data). Our experiments consider two major deep learning architectures. We observe that using multi-modal temporal inputs outperforms single-modal temporal inputs across all metrics, achieving a peak performance of 60.3% in F1 score for the 2023 wildfire season, a season never seen during model training. This demonstrates the

*Corresponding author: hugo.porta@epfl.ch

potential of multi-modal deep learning models for wildfire forecasting at high-resolution and continental scale.

Keywords: Wildfire Forecasting, Benchmark Dataset, Multi-modal Learning, Deep Learning, Boreal Ecosystem

1. Introduction

As climate change accelerates, forests represent a key ecosystem as they act as one of the main terrestrial carbon sinks (Keenan and Williams, 2018), a shelter for a major part of Earth’s biodiversity (Lindenmayer and Franklin, 2013) during this new era of great extinction (Barnosky et al., 2011), and a critical environment for numerous fragile human communities (Fernández-Llamazares et al., 2021). Climate change endangers the role of forests as a carbon sink: it has been observed that several forest biomes are at risk of shifting from carbon sinks to carbon emitters (Pan et al., 2024). In particular, the boreal ecosystem is a subarctic biome in the high northern latitudes characterized by coniferous and mixed deciduous-coniferous forests. As the northernmost forest on the planet, boreal forests span 58% of Canada’s land mass and are present across 7 other countries. To date, boreal forests represent one of the largest terrestrial carbon sinks, with approximately 367.3 petagrams to 1715.8 petagrams of carbon (Bradshaw and Warkentin, 2015). However, they are at risk of permafrost thaw due to land impacts (Li et al., 2021) and are increasingly subject to long and devastating wildfire seasons (McCarty et al., 2021).

Wildfires greatly threaten many forest ecosystems due to the rapid shift in climate change-driven fire regimes. Indeed, despite a decreasing trend in the global burned area (mainly driven by a decrease of human-caused fires in African grasslands), (Bowman et al., 2020), areas burned by forest fires have seen a steady yearly increase of $\sim 5\%$ since 2001 (Tyukavina et al., 2022). In addition, forest fire events are burning longer and covering larger areas as extreme wildfire events’ frequency increases (Cunningham et al., 2024). As a consequence, wildfire CO₂ emissions reached 24% of the total global emissions in 2023, corresponding to 8.6 Gt of CO₂ (Jones et al., 2024; Liu et al., 2024). The observed amplification in wildfire severity is particularly true for the boreal ecosystem, representing roughly 70% of the fire-related tree cover loss (Tyukavina et al., 2022) and where single wildfire events, like those during the 2023 Canadian wildfires season, can compete with annual

emissions of major industrialized nations (Byrne et al., 2024). Locally, boreal wildfires have a direct impact on the land surface as they directly enhance permafrost thaw (Li et al., 2021; Zhao et al., 2024), and also contribute to vegetation shifts to more fire-prone grassland-/steppe-dominant landscapes, as well as dry peat (Zhao et al., 2024; McCarty et al., 2021). Those effects on local ecosystems, combined with wildfire CO₂ emissions, create a positive feedback mechanism fueling climate change. Finally, boreal wildfires emit large amounts of aerosols into the atmosphere, which can directly impact ice melt in the Arctic (Schmale et al., 2021) and are dangerous for public health, both locally and after smoke transportation thousands of kilometers away (Weilhammer et al., 2021).

The use of remote sensing data to map and monitor wildfires has expanded, with studies considering satellite-based observations of vegetative fuel conditions, individual fire events, and the impacts of smoke. Researchers have developed numerous wildfire tools, with three main use cases focused on the different phases of a wildfire: before a wildfire occurs (pre-fire), during a wildfire (active fire), and after (post-fire). For active fires, satellite products and models detect active fire "hotspots" in near real-time (de Almeida Pereira et al., 2021; Ružička et al., 2022) or predict wildfire spread (Huot et al., 2022; Hoang et al., 2022), providing precious tools for wildfire management and decision-making. In the aftermath of wildfires (i.e. post-fire), methods to precisely segment the perimeter of burned areas (Rashkovetsky et al., 2021; Zhang et al., 2022) were developed to evaluate wildfires emissions, from CO₂ to black carbon, and estimate the impact of wildfires on the local ecosystem, natural resources, and communities. This study focuses on the first category (pre-fire) for wildfire prevention, shaped from a methodological perspective as a forecasting task. Wildfire forecasting, often referred to as wildfire susceptibility or likelihood modeling (Pelletier et al., 2023; Zhang et al., 2021), aims to predict the spatial probability of a wildfire occurring in a given time horizon and at a given spatial resolution (Prapas et al., 2022). This is done by producing wildfire probability maps. Wildfire forecasting is particularly useful for wildfire management by supporting staff and resource planning (Wotton, 2009).

Wildfire forecasting is, by definition, a difficult task since it seeks to represent a complex and stochastic phenomenon. Fire susceptibility depends on several drivers: **i)** hydrometeorological conditions are the main variables that impact the suitability of vegetative fuels for combustion (ie, 'dryness') and fire propagation (Krawchuk et al., 2009). Flammability is also directly

linked to **ii**) the available biomass for combustion, which depends on **iii**) the type of vegetation and other indicators such as **iv**) dead or live fuel moisture (Krawchuk et al., 2009). Climate change makes those predictors for wildfire occurrence non-stationary. For example, meteorological patterns are highly variable in the boreal biome, which can lead to extreme fire seasons (McCarty et al., 2021). In addition, numerous vegetation changes have been observed or predicted, such as permafrost thaw (Li et al., 2021; Zhao et al., 2024), peatland destruction (Bourgeau-Chavez et al., 2022), or a shift from coniferous to deciduous forest (McCarty et al., 2021). Moreover, for effective wildfire forecasting, it is necessary to estimate **v**) the probability of ignition caused by humans or lightning (Pérez-Invernón et al., 2023) through proxies such as the proximity to human settlements. This variability implies that for similar environmental conditions, a wildfire may or may not occur based on latent variables for the model, which makes wildfire forecasting an especially complex task where ignition, even from lightning-only, is hard to model (Coughlan et al., 2021; Bates et al., 2021).

Historically, wildfire forecasting was performed by producing fire weather indices, such as the Canadian Forest Fire Weather Index (FWI) or the National Fire Danger Rating System (NFDRS), which are mainly driven by meteorological and fuel moisture data. Fire weather indices aim to represent complex relationships between fire predictors through constraint equations based on assumptions that can lack robustness, such as focusing on specific forest types (e.g. "Pinus Banksiana") or not taking into consideration the topography which can lead to necessary re-calibrations of the indexes for specific areas (Steinfeld et al., 2022; De Jong et al., 2016). Moreover, due to limitations in weather reanalysis or forecast data, fire weather indexes are often limited to short-term temporal horizons and coarse resolution. For instance, across Canada, the FWI has limitations in properly identifying the hydrometeorological conditions for combustion across all land cover types, and particularly so in peatlands (Waddington et al., 2012). Moreover, those indices cannot approximate the stochastic character of wildfire occurrence as they focus on flammability conditions. In parallel, traditional machine learning (ML) algorithms based on handcrafted features were proposed in (Martell et al., 1987, 1989) to identify drivers linked to wildfire occurrence, such as hydrometeorological conditions and human activities. These ML algorithms are limited in their ability to represent complex predictor relationships and possible spatio-temporal patterns, mostly because of the rigidity of the features used. Nevertheless, these methods are still widely used (Buch et al.,

2023; Rodrigues et al., 2022) even in remote sensing (Pelletier et al., 2023; Chowdhury and Hassan, 2015).

The growing availability of open remote sensing data (Reichstein et al., 2019; Camps-Valls et al., 2021), which enables the monitoring of large and remote regions, now allows mapping the drivers of fire susceptibility. This contributed to the emergence of wildfire forecasting models leveraging remote sensing imagery with traditional ML (Pelletier et al., 2023; Chowdhury and Hassan, 2015) and deep learning (DL) (Yang et al., 2021) methods. Different model designs have been used in the recent literature¹: for one-dimensional inputs, the method of choice is the Multi-Layer Perceptron (MLP) (Buch et al., 2023; Bakke et al., 2023; Milanović et al., 2020), while for temporal-only inputs Long Short Term Memory (LSTM) networks have been proposed (Natekar et al., 2021) due to their ability to process sequences (e.g time series) by passing information along the sequence. When considering spatial inputs, convolutional neural networks (CNN) and vision transformer (ViT) have been explored (Prapas et al., 2022, 2023). Finally, for spatio-temporal data, architectures like convolutional LSTM (ConvLSTM) (Kondylatos et al., 2022; Huot et al., 2020; Prapas et al., 2021; Bali et al., 2021), which join the sequence processing abilities of LSTM networks to the spatial awareness of CNNs, have been proposed. There is no clear consensus on the best model to use, as results seem to vary depending on the dataset characteristics (Kondylatos et al., 2022; Huot et al., 2020; Prapas et al., 2021; Jain et al., 2020), region of interest, forecast horizon, and predictors list. In terms of data, most methods leverage hydrometeorological predictors, from reanalysis data like ERA5 or weather stations with spatial resolution varying from ~ 27 km to 4 km. They also leverage remote sensing products linked to vegetation at higher resolution (up to 500 m) and static factors linked to land cover and human activities (Kondylatos et al., 2022; Prapas et al., 2021; Bakke et al., 2023; Prapas et al., 2022; Bali et al., 2021). Those predictors are then re-sampled according to a target output resolution for the wildfire probability maps, varying from 0.25° for global applications (Bakke et al., 2023; Prapas et al., 2022) to up to 1 km for more localized regions (Kondylatos et al., 2022; Huot et al., 2020; Prapas et al., 2021). For instance, in the context of large countries such as Canada, which spans thousands of kilometers, the

¹We will limit this review to neural network-based approaches, which are the closest to our proposition.

coarse output resolution of current wildfire probability maps is $\sim 0.1^\circ$ (Bali et al., 2021). This represents an important limitation of current wildfire forecasting models and datasets, as such coarse wildfire probability maps prevent wildfire management from properly allocating resources globally and lead to the underestimation of potential smaller wildfires.

In this paper, we propose a large-scale, multi-modal, and spatio-temporal dataset to train high-resolution wildfire forecasting models and identify the best approach. First, we propose a benchmark dataset for high-resolution wildfire forecasting: CanadaFireSat² available on the HuggingFace Hub, which allows the forecasting of wildfire risk at a spatial resolution of 100 m over the entirety of Canada. CanadaFireSat allows us to go beyond what was possible with previous datasets, such as (Huot et al., 2020) or (Prapas et al., 2021), both with a target resolution of 1 km over the U.S. and the Eastern Mediterranean region, respectively. We enable high-resolution wildfire forecasting by resorting to temporal series of multi-spectral satellite images (multi-spectral satellite images have been shown to be predictive of wildfires (Yang et al., 2021; Pelletier et al., 2023)), which complement temporal series of environmental drivers from both reanalysis data (ERA5) and coarse resolution satellite products (MODIS) (Prapas et al., 2022), as shown in Figure 1. In the proposed CanadaFireSat, the role of multi-spectral images is to provide high-resolution information on local fire drivers thanks to the 10 m resolution bands for Red, Green, Blue, and near infrared (NIR) of Sentinel-2. The environmental variables represent commonly-used fire drivers, from temperature to the normalized difference vegetation index (NDVI) at coarser multi-scale resolutions. Secondly, in this paper, we demonstrate the potential of learning multi-modal models for wildfire forecasting by benchmarking two state-of-the-art computer vision architectures on CanadaFireSat: ResNet (He et al., 2016) and ViT (Dosovitskiy, 2020). We consider three settings with varying inputs modality: **1** satellite images only (Sentinel-2 at 10m), **2** environmental predictors only (ERA5 at 11km, FWI at 0.25° , MODIS at 1km and 500m), and **3** satellite and environmental data, as represented in Figure 1.

Our results on CanadaFireSat demonstrate that deep learning models can

²Code for the data generation and the model benchmarking can be accessed, respectively, at github.com/eceo-epfl/CanadaFireSat-Data and github.com/eceo-epfl/CanadaFireSat-Model

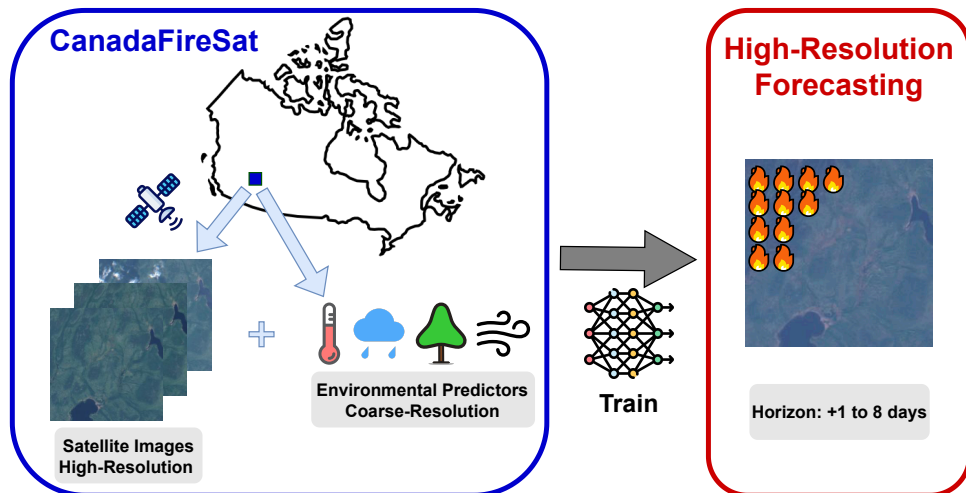


Figure 1: Representation of the CanadaFireSat benchmark and the high-resolution wildfire forecasting task.

outperform a knowledge-driven baseline (FWI), in both normal and extreme fire seasons by up to +15% in PRAUC and +11% in F1 score. Moreover, we showcase the importance of multi-modal approaches for enhanced performance, and that convolution-based models outperform transformer architectures across all setups on CanadaFireSat. Our best-performing model: ResNet-50 in setting ③ **satellite and environmental data**, reaches a top performance of 51.2 F1 score and 46.1 PRAUC on the 2022 validation set and up to 60.3 F1 score and 57.0 in PRAUC for the extreme fire season year of 2023. In comparison, the best performing TeleVit model (Prapas et al., 2023) on the SeasFire global benchmark reaches $\sim 62\%$ PRAUC on their test set for the same 8-day horizon and at a resolution of 0.25° , a resolution 270 times coarser than CanadaFireSat. Even if not directly comparable, these results showcase the great potential of high-resolution wildfire forecasting via multi-modal models.

2. CanadaFireSat Dataset

In this section, we present CanadaFireSat, a benchmark dataset for high-resolution wildfire forecasting. First, we describe the sampling scheme for the selection of positive and negative data samples in Section 2.1. Then, in Section 2.2 we provide the set of predictors that we extracted and combined to

Statistic	Value
Total Samples	177,801
Target Spatial Resolution	100 m
Region Coverage	Canada
Temporal Coverage	2016 - 2023
Sample Area Size	2.64 km × 2.64 km
Fire Occurrence Rate	39% of samples
Total Fire Patches	16% of patches
Training Set (2016-2021)	78,030 samples
Validation Set (2022)	14,329 samples
Test Set (2023)	85,442 samples
Sentinel-2 Temporal Median Coverage	55 days (8 images)
Number of Environmental Predictors	58
Data Sources	ERA5, MODIS, CEMS

Table 1: Main Statistics of the CanadaFireSat Dataset

build our multi-modal learning benchmark for high-resolution wildfire forecasting. Table 1 provides the key information on this dataset.

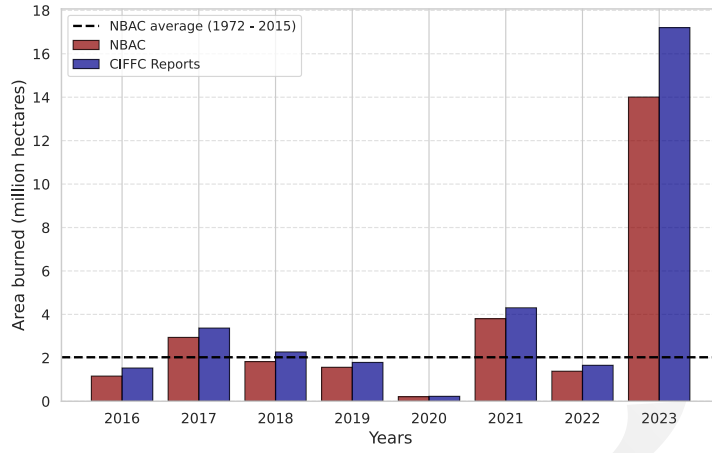
2.1. Sample Identification

Canada being a large country, we sampled areas across all provinces and territories. As our fire labels are binary, we sampled the dataset as a series of positive and negative examples. For fire (*positive*) sample identification, we first extract all fires occurring between 2015 and 2023, as described in Section 2.1.1. Then, samples not including any fire event (*negative*) are sampled across the same period for all provinces and territories, depending on their fire weather index and acquisition dates, as detailed in Section 2.1.2.

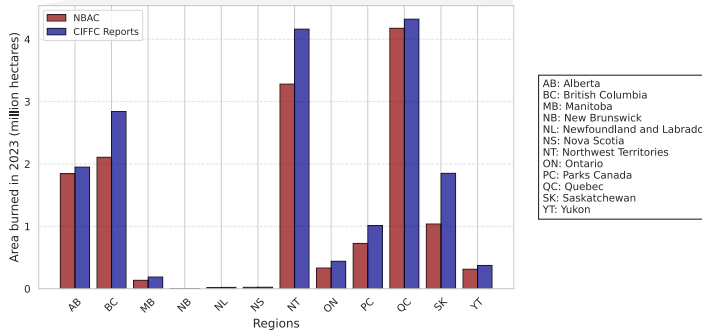
2.1.1. Positive Samples

Fire samples in our CanadaFireSat dataset are identified based on the fire polygons of the National Burned Area Composite³ (NBAC) (Hall et al., 2020) from the Canadian National Fire Database. NBAC has been compiled annually since 1972 and integrates data from Natural Resources Canada, provincial and territorial agencies, and Parks Canada, using a rule-based approach to select the most accurate burned area perimeter delineations based

³Available at <https://cwfis.cfs.nrcan.gc.ca/datamart/metadata/nbac>



(a)



(b)

Figure 2: Burned area in Canada in millions of hectares extracted from NBAC compared to reported values from the Canadian Interagency Forest Fire Centre (CIFFC). (a) shows the annual burned area for the entire Canada from 2016 to 2023, while (b) reports the per-region burned area for 2023 only.

on post-event satellite imagery. We focus on all fires since 2015 (the launch of the Sentinel-2 satellites), with no restriction on ignition sources or other fire metadata. In Figure 2a, we report the yearly average burned area for this period from NBAC, with 2022 reaching 1.38 mha burned and 2023 reaching 14.01 mha burned. This outlines the two different regimes of wildfire season for our validation (2022) and test (2023) sets compared to the average from

1972 to 2015 of ~ 2.03 mha. In other words, 2023 was an exceptional fire season. We compared such statistics against the average burned area reported by the Canadian Interagency Forest Fire Centre (CIFFC) for 2023: 17 mha. The difference between CIFFC and NBAC reported burned area has multiple explanations. First, the CIFFC statistics are not standardized across all territorial fire management agencies, contrary to NBAC. This is directly linked to data collection timelines, as CIFFC may provide near-real-time estimates while NBAC is compiled up to 6 months after the calendar year, leaving more room for comprehensive post-fire analysis. In Figure 2b, we also break down the regional burned area statistic for the 2023 wildfire season where the most impacted provinces and territories were Québec, Northwest Territories⁴, and British Columbia. It should be noted that British Columbia is often impacted by severe wildfire seasons, and often leads Canada in terms of total burned area, but 2023 was not a record year for this province. Also, we note that the most impacted regions are those with the strongest discrepancies between reported numbers from CIFFC and NBAC.

Positive samples for the CanadaFireSat dataset are extracted from the NBAC fire polygons through two aggregation processes. First, through a spatial aggregation on a $2.8 \text{ km} \times 2.8 \text{ km}$ grid over Canada, where positive samples are identified as the grid entries intersecting the fire polygons. We used a small buffer around the $2.64 \text{ km} \times 2.64 \text{ km}$ tiles to avoid any potential overlap between samples due to data imprecision. Second, a temporal aggregation is performed in two steps: 1) all fires temporally overlapping inside a grid entry are accounted as a single fire occurring from the first start date to the last end date, and 2) leveraging the 8-day temporal grid from products such as NDVI from MODIS (starting each year at the 1st of January) we aggregate all fires within a spatial grid entry occurring during the same 8-day window. This is done to build our 8-day wildfire forecasting benchmark where, for a given time-step t , our model should predict the probability of a fire occurring in the next 8-days, i.e. from t to $t + 7$ included, leveraging predictors (both satellite and environmental) from $t - \Delta t$ to $t - 1$. In Figure 3a, we showcase the spatial distribution of positive samples across Canada, for a total of $n_{pos} = 88'110$ samples before any post-processing (detailed in Section 2.2). Outside of British Columbia, most fires occur in the boreal

⁴Natural Resources Canada, that provides NBAC data includes Nunavut fires in Northwest Territories statistics.

ecosystem. This pattern is very visible across Alberta, Saskatchewan, and Manitoba, where the Great Plains in southern portions of these provinces show little to no fires compared to the boreal forest in the north.

2.1.2. Negative Samples

As we aim to build our benchmark on multi-modal inputs, including satellite image time series, we are limited in storage to densely sample Canada over the whole period from 2015 to 2023. Therefore, we sampled a negative set of size $n_{neg} = 2 \cdot n_{pos}$ to emulate a degree of imbalance, following other datasets on wildfire forecasting (Huot et al., 2020; Prapas et al., 2021; Kondylatos et al., 2022). We sample from the same grid defined in Section 2.1.1, $G_{y,r}$, for each year y between the first and last occurring fires during that year (so beyond the wildfire season), and across all regions r . For a given year $y > 2015$ and region r we avoid locations where a fire occurred in the previous years: $\bigcup_{i=2015}^{y-1} F_{i,r}$, or locations that were already selected as negative samples in the previous years: $\bigcup_{i=2015}^{y-1} N_{i,r}$. Our negative set for a given region and year can be defined as such:

$$N_{y,r} \sim S_{y,r} = \{x \in G_{y,r} \mid x \notin \bigcup_{i=2015}^{y-1} F_{i,r} \wedge x \notin \bigcup_{i=2015}^{y-1} N_{i,r}\} \quad (1)$$

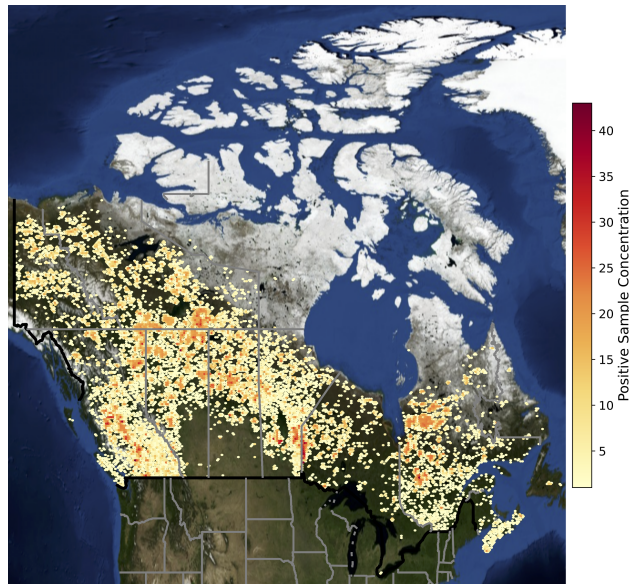
where $N_{y,r}$ is the set of negative samples and $S_{y,r}$ the set of potential locations in the grid. We sample $N_{y,r}$ uniformly across levels (defined by buckets) of the fire weather index: FWI:

$$P_{FWI}(x|N_{y,r}) \propto P_{FWI}(x|S_{y,r}) \quad (2)$$

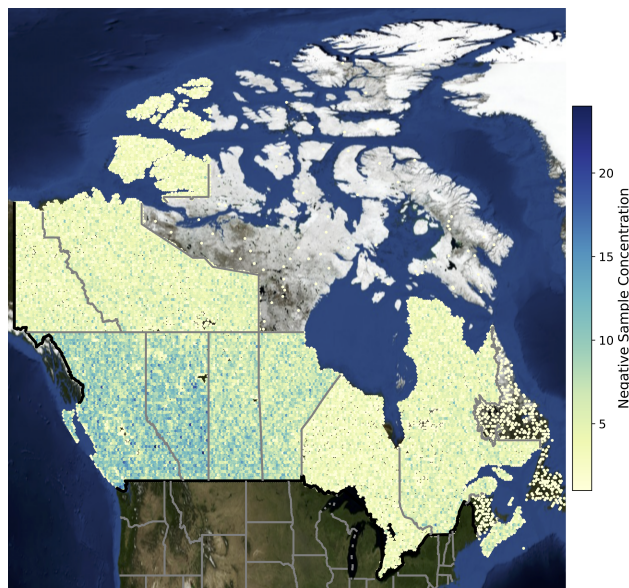
In practice, this is done by partitioning the FWI distribution into ten buckets (or bins): $[B_1, \dots, B_{10}]$ across the FWI quantiles $[Q_1, \dots, Q_9]$ such that each bucket contains approximately 10% of the observations, and uniformly sampling across those buckets for $N_{y,r}$. In practice, each bucket B_l is defined as a subset of the FWI range:

$$B_l = \{x \in \text{FWI} \mid Q_{l-1} < x \leq Q_l\}, \quad \text{for } l = 1, \dots, 10 \quad (3)$$

where $Q_0 = 0$, and $Q_{10} = +\text{inf}$ are the bounds of the FWI range. This way, the negative population is representative of all fire weather conditions for each region and year, including cases where a high FWI was predicted, but no fire was observed.



(a) Positive sample concentration across the period 2015-2023



(b) Negative sample concentration across the period 2015-2023

Figure 3: Distribution of our positive samples (containing burned area) and negative samples (following our FWI-based sampling strategy) from 2015-2023, before any post-processing.

In Figure 4a, we present the annual FWI mean for our negative sample set. We see that up to the bucket: 4 with a FWI mean of $\overline{\text{FWI}} = 0.62$, most negative samples will have an FWI close to 0, as the FWI distribution of available locations for negative samples consistently presents an important peak in this range. This is representative of the FWI conditions across all regions of Canada between the first and last fires of each year. Furthermore, we show in Figure 4b and 4c that across two commonly impacted regions by wildfires, Alberta and Northwest Territories, there are strong differences in FWI bucket mean value between regions, with the delta for the top bucket reaching up to ~ 14 in 2021. This can be explained by the higher latitude of the Northwest Territories compared to Alberta and the presence of permafrost in their northernmost areas.

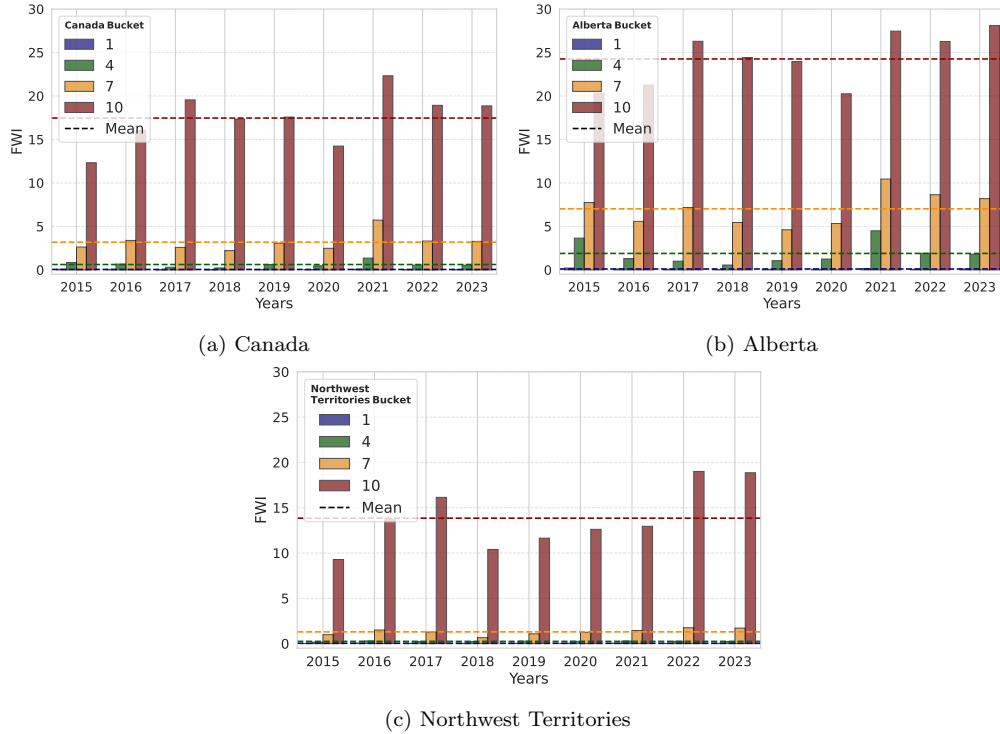


Figure 4: Annual FWI mean over four buckets: $\{1, 4, 7, 10\}$ across Canada, Alberta, and Northwest Territories.

Figure 3b presents the spatial distribution of the sampled negative locations across all years: it shows that, per region, the negative samples are well spread spatially, contrary to the positive samples, as we aim to represent

the complete patterns of fire danger conditions. British Columbia, Alberta, Saskatchewan, and Manitoba contain the highest concentration of negative samples in certain areas due to the high concentration of fires in those regions (negative samples are sampled twice as much as positive ones). On the contrary, Nunavut, Newfoundland and Labrador, and New Brunswick are less densely sampled due to a lack of fires during the analyzed period. We select in total $n_{neg} = 176,650$ negative samples. Note that some of these samples will be filtered out through the post-processing procedure described in Section 2.2. In Section 4.1, we will also introduce an adversarial sampling strategy for the negative samples to study the lower-bound performance of wildfire forecasting models in such a challenging scenario for the extreme year 2023.

2.2. Predictors

The predictors used in CanadaFireSat fall into two categories: satellite image time series and environmental data. We begin by describing the satellite image time series, a novel component that enhances high-resolution wildfire forecasting by complementing the more commonly used environmental data. We then present the environmental data.

2.2.1. Satellite Image Time Series

To be able to forecast wildfires at a pixel resolution of 100 m, we need high-resolution information. However, hydrometeorological fire danger predictors cannot be found at 100 m resolution for the entirety of Canada. Therefore, we investigate the potential of multi-spectral high-resolution satellite images as proxies for fire predictors following previous literature (Pelletier et al., 2023; Yang et al., 2021). We use the 13 bands from Sentinel-2 (S2) L1C harmonized data as proxies to several known fire predictors (NDVI, soil moisture, ...). We use the L1C products as they are directly available for the whole period 2015-2023 without any need for further processing. Moreover, we extract temporal data to better estimate the impact of changes in the hydrometeorological conditions on the local ecosystem.

For a given sample $x_t \in G_{y,r}$ (the $2.8 \text{ km} \times 2.8 \text{ km}$ grid over Canada), we downloaded all the full (no missing values) S2 images of size $2.64 \text{ km} \times 2.64 \text{ km}$ centered within each grid cell x_t between the date $t-64$ days and $t-1$ day. We excluded images with a cloud cover above 40%. This represents 13 images, given the average revisit time of 5 days for S2. To avoid artifacts, we use a lossless compression: LZW, and we multiplied each band intensity by a factor

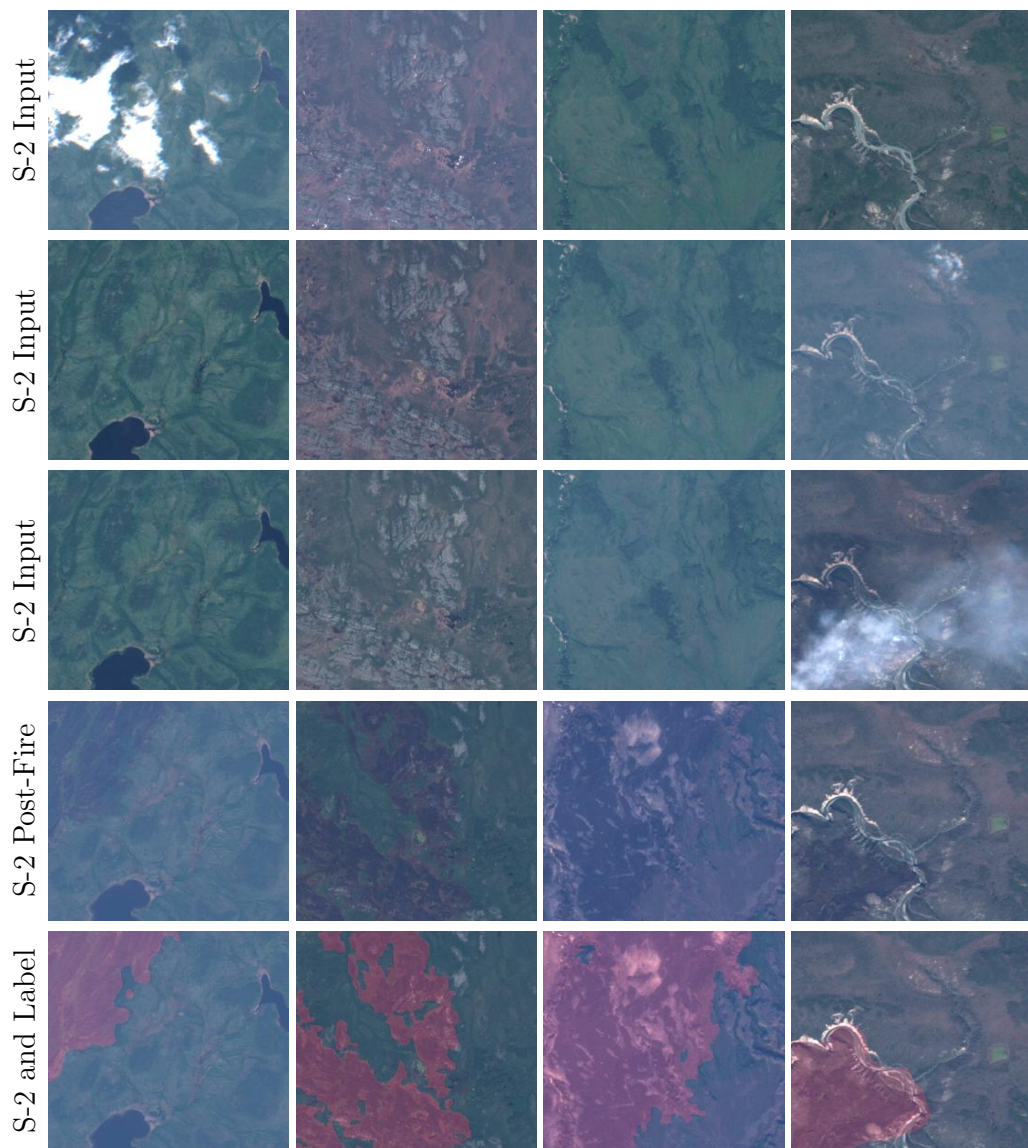


Figure 5: **Row 1-3** Samples of Sentinel-2 input time series for 4 locations in Canada, with only the RGB bands with rescaled intensity. **Row 4** Sentinel-2 images after the fire occurred. **Row 5** Fire polygons used as labels with the Sentinel-2 images post-fire.

$1e^{-4}$ to then rescale the values to 8-bit unsigned integers. Once all S2 images were extracted, a second filter on cloud coverage was applied, based on the S2 cloud probability product, but focusing only on the region of interest. After this filtering, the samples x_t with less than three S2 images or covering a period of less than 40 days were removed. Finally, as multiple S2 tiles can cover a sample x_t , we kept the tile with the most valid images for this sample. The final positive sample set after filtering is of size 69,876 \sim 79% of the original set, and the negative sample set is of size 107,925 \sim 61% of the original set.

The fire polygons associated with each positive sample are rasterized based on the B3 band of the S2 image that preceded the start of the fire. This process outputs binary maps of size 264×264 pixels at a resolution of 10 m that will then be downscale during training. Figure 5 shows examples of S2 image time series from the positive set and the expected output when a fire occurred.

2.2.2. Environmental Predictors

Fire weather indices and most wildfire forecast models rely on well-known hydrometeorological drivers such as temperature, precipitation, and soil moisture. Some forecast models also leverage vegetation indices such as NDVI, EVI, or LAI. Since we aim for high-resolution wildfire forecasting, those predictors at coarse resolutions could be seen as unnecessary compared to satellite image time series. Nonetheless, we argue that despite an important difference in resolutions between those predictors and our target outputs, multi-modal methods can benefit from coarse environmental predictors, as those are directly linked to fire probability.

For this purpose, we extract a series of environmental indices at coarse resolution, summarized in Table 2.

- First, we extract five different MODIS products that describe the vegetation state and temperature at moderate-to-coarse-resolution: 500 m and 1 km. Vegetation indices are 8-day or 16-day composites, which similarly to SeasFire (Prapas et al., 2022), drive the temporal aggregation over 8 days of the other environmental predictors, and the NBAC burned area polygons.
- We also extracted 12 hydrometeorological drivers from ERA5-Land daily (detailed in Table 2) at coarse-resolution: 11 km, and aggregated those variables through mean, max, and min operators on the

8-day temporal grid defined by MODIS. We extend this set of predictors with three predictors: relative humidity, vapor pressure deficit, and wind speed, computed locally from ERA5 data.

- Lastly, we leverage indices related to fire danger from the Copernicus Emergency Management Service (CEMS): fire weather index, also used in negative sampling, and drought code, both from the Canadian Forest Fire Weather Index. This data is the coarsest of all our environmental predictors with a resolution of 0.25° for both latitude and longitude.

These predictors are then post-processed to set to NaN any extreme values and aligned both spatially and non-spatially with our positive and negative samples. Similar to the satellite image time series, for each sample x_t , we extract the environmental predictors from $t - 64$ days to $t - 1$ day. The non-spatial alignment is done via the weighted average of a given predictor over the target grid cell. The spatial alignment is done for each predictor by extracting a small window of data centered on x_t . The window size varies depending on the source resolution. We extract windows of dimension $(32, 32)$ for MODIS products at 500 m and $(16, 16)$ for MODIS product at 1km. Moreover, for ERA5-Land data, we extract windows of size $(32, 32)$, and $(13, 13)$ for CEMS.

3. Methods

To demonstrate the feasibility of forecasting wildfires at 100 m resolution, we benchmark two deep learning architectures on the proposed CanadaFire-Sat dataset. We chose a CNN and a Transformer as representative computer vision models, whose encodings are used to forecast wildfire probability at an 8-day horizon. To account for multi-modal interactions, models are trained in three different settings: ❶ **satellite images only** (Sentinel-2), ❷ **environmental predictors only** (ERA5, CEMS, MODIS), and when both ❸ **satellite and environmental data** are available. Detailed information on the settings can be found in Table 3.

Across our experiments, the original labels are re-scaled to a resolution of $100\text{ m} \times 100\text{ m}$, by labeling a patch with the binary class *fire* if any pixel, within the patch, is labeled as burned. As a consequence, for CanadaFire-Sat, wildfire forecasting is framed as a dense binary classification task (*fire* vs. *no fire*) at the patch level that we name **binary patch classification**.

Dataset	Name	Units	Aggregation	Resolution	Source
MODIS	NDVI	-	16-day composite	500 m	Google Earth Engine
	EVI	-	16-day composite	500 m	Google Earth Engine
	LST Day (1km)	K	8-day mean, max, min	1 km	Google Earth Engine
	FPAR	-	8-day composite	500 m	Google Earth Engine
	LAI	-	8-day composite	500 m	Google Earth Engine
ERA5-Land	Surface Pressure	Pa	8-day mean, max, min	11.1 km	Google Earth Engine
	Total Precipitation Sum	m	8-day mean, max, min	11.1 km	Google Earth Engine
	Skin Temperature	K	8-day mean, max, min	11.1 km	Google Earth Engine
	U Component of Wind (10m)	m/s	8-day mean, max, min	11.1 km	Google Earth Engine
	V Component of Wind (10m)	m/s	8-day mean, max, min	11.1 km	Google Earth Engine
	Temperature (2m)	K	8-day mean, max, min	11.1 km	Google Earth Engine
	Temperature (2m, Max)	K	8-day mean, max, min	11.1 km	Google Earth Engine
	Temperature (2m, Min)	K	8-day mean, max, min	11.1 km	Google Earth Engine
	Surface Net Solar Radiation Sum	J/m ²	8-day mean, max, min	11.1 km	Google Earth Engine
	Surface Solar Radiation Downwards Sum	J/m ²	8-day mean, max, min	11.1 km	Google Earth Engine
	Volumetric Soil Water Layer 1	m ³ /m ³	8-day mean, max, min	11.1 km	Google Earth Engine
	Dewpoint Temperature (2m)	K	8-day mean, max, min	11.1 km	Google Earth Engine
	Relative Humidity	%	8-day mean, max, min	11.1 km	Own Calculation
	Vapor Pressure Deficit	hPa	8-day mean, max, min	11.1 km	Own Calculation
Wind Speed (10m)	m/s	8-day mean, max, min	11.1 km	Own Calculation	
CEMS	Drought Code	-	8-day mean, max, min	0.25° (28 km)	CEMS Early Warning Data Store
	Fire Weather Index	-	8-day mean, max, min	0.25° (28 km)	CEMS Early Warning Data Store

Table 2: Overview of the environmental predictors.

Setting	Source	Format	Type
①	Sentinel-2	Spatial	Multi-Spectral Images
②	MODIS	Spatial	Environmental Products
	ERA5-Land CEMS	Spatial Spatial	Climate Reanalysis Fire Indices
③	Sentinel-2	Spatial	Multi-Spectral Images
	MODIS	Tabular	Environmental Products
	ERA5-Land CEMS	Tabular Tabular	Climate Reanalysis Fire Indices

Table 3: Descriptions of the modality settings for the training of the wildfire forecasting models.

Moreover, as satellite image time series are not evenly spaced due to cloud cover, we add as complementary information the day of the year for all our predictors. Other details on the experimental setup for all architectures can be found in Appendix B. Moreover, we analyze the impact of satellite image time series on model performance in Appendix C.

3.1. CNN-based Architecture

In the CNN-based architecture, satellite image time series are processed in a factorized manner: first spatially and then temporally, for both settings **1** satellite images only and **3** satellite and environmental data, as shown in Figure A.12 and Figure 6, respectively. For a given satellite image time series $x_{1:T} = \{x_t\}_{t=1}^T$, $x_t \in \mathbb{R}^{H \times W \times C}$ with C the number bands and the day of the year, and T a fixed number of time steps, each image x_t is first encoded independently by a ResNet-50 pre-trained on ImageNet (He et al., 2016): $f(x_t) = \{z_{i,t}\}_{i=1}^{N_S}$, $z_{i,t} \in \mathbb{R}^{H_i \times W_i \times D_i}$, which outputs $N_S = 3$ feature maps of channel dimension D_i , each feature map corresponds to a different scale. The encoding of all time steps is done in parallel, and each scale-specific feature map: $z_{i,t}$, is concatenated independently for each scale across the temporal axis: $z_{i,1:T} = \{z_{i,t}\}_{t=1}^T$. Then, the spatio-temporal encoding is done via one ConvLSTM model per scale. By extracting the last hidden state from each ConvLSTM: g_i , we obtain feature maps $g_i(z_{i,1:T}) = s_i$, $s_i \in \mathbb{R}^{H_i \times W_i \times D'_i}$ at 3 different scales with channel dimension $D'_i < D_i$, providing multiple levels of contextual information.

In setting **1** satellite images only, our final multi-scale feature maps $\{s_i\}_{i=1}^{N_S}$ are passed to a U-Net-like decoder. The output of the decoder is interpolated to the dimensions of the label feature map: $H_{\text{fire}} = W_{\text{fire}} = \frac{H}{10} = \frac{W}{10}$ to match the patch resolution. This is finally passed to binary patch classification layer to output the class probabilities: $h(\{s_i\}_{i=1}^{N_S}) = \hat{y} \in [0, 1]^{H_{\text{fire}} \times W_{\text{fire}} \times 2}$, with h the function representing the decoder, interpolation, and patch classification layer.

In the multi-modal setting **3** satellite and environmental data, displayed in Figure 6, the above architecture is extended to process in parallel the time series of non-spatial environmental predictors $x_{\text{env},1:T_{\text{env}}} = \{x_{\text{env},t}\}_{t=1}^{T_{\text{env}}}$, $x_{\text{env},t} \in \mathbb{R}^{N_{\text{env}}}$ with N_{env} the number of environmental predictors and T_{env} a fixed number of time steps. Following (Gorishniy et al., 2022) for tabular data encoding, each environmental predictor is projected to a high-dimension space through specific MLP layers: $\forall j \in \{1, \dots, N_{\text{env}}\}$, $f_{\text{env},j}(x_{\text{env},t}^j) = z_{\text{env},t}^j$, $z_{\text{env},t}^j \in \mathbb{R}^{D_{\text{env}}}$. The projected features are then averaged across the N_{env}

dimension to obtain $z_{\text{env},1:T_{\text{env}}} \in \mathbb{R}^{D_{\text{env}} \times T_{\text{env}}}$ and passed to an LSTM model for temporal encoding $g_{\text{env}}(z_{\text{env},1:T_{\text{env}}}) = s_{\text{env}}$, $s_{\text{env}} \in \mathbb{R}^{D_{\text{env}}}$ for the final environmental encoded feature. This one-dimensional vector is replicated spatially and concatenated with the final feature map from the U-Net-like decoder before the patch classification layer: $h(\{s_i\}_{i=1}^{N_S}, s_{\text{env}}) = \hat{y} \in [0, 1]^{H_{\text{fire}} \times W_{\text{fire}} \times 2}$.

For setting **2** environmental predictors only, where the model is trained using only environmental predictors at a resolution varying from 500 m up to 28 km (see Table 2), we first split the predictors into two groups: mid-resolution inputs $x_{\text{mid},1:T_{\text{env}}} = \{x_{\text{mid},t}\}_{t=1}^{T_{\text{env}}}$, $x_{\text{mid},t} \in \mathbb{R}^{H_{\text{mid}} \times W_{\text{mid}} \times N_{\text{mid}}}$ for all MODIS data, and low-resolution inputs for all ERA5 and CEMS data: $x_{\text{low},1:T_{\text{env}}} = \{x_{\text{low},t}\}_{t=1}^{T_{\text{env}}}$, $x_{\text{low},t} \in \mathbb{R}^{H_{\text{low}} \times W_{\text{low}} \times N_{\text{low}}}$. In this setting, we leverage spatial environmental inputs and not tabular to compensate for the absence of high-resolution satellite imagery (Sentinel-2), providing spatial context for settings **1** satellite images only and **3** satellite and environmental data. In each group, as not all predictors have the same spatial resolution (see Table 2), we upsampled all predictors to the highest available resolution. Details on the different spatial dimensions for each group can be found in the Appendix B. We will partially modify the architecture from setting **3** satellite and environmental data, as shown in Figure A.13. First, mid-resolution inputs are used as an alternative to satellite image time series. In practice, all the satellite image processing model components stay the same for the mid-resolution inputs group: the spatial encoding f , the scale-specific temporal encoding g_i , and the final head h (corresponding to the decoder, interpolation layer, and patch classification layer). We simply extend the number of multi-scale feature maps to $N_S = 5$ because of the lower resolution of the input data. Moreover, we exchange ConvLSTM with LSTM when the output feature maps from f become one-dimensional (for $i = 5$). The second branch of the model is adapted to process spatial data for the low-resolution inputs group. We use a smaller pre-trained CNN architecture to encode independently each time step similarly to satellite images: ResNet-18 (He et al., 2016): $f_{\text{low}}(x_{\text{low},t}) = z_{\text{low},t}$, $z_{\text{low},t} \in \mathbb{R}^{D_{\text{low}}}$. The spatial encoding for this input resolution outputs a single-scale 1-D vector. The temporally concatenated features $z_{\text{low},1:T_{\text{env}}} \in \mathbb{R}^{D_{\text{low}} \times T_{\text{env}}}$ are passed to an LSTM model $g_{\text{low}}(z_{\text{low},1:T_{\text{env}}}) = s_{\text{low}}$, $s_{\text{low}} \in \mathbb{R}^{D'_{\text{low}}}$ to obtain low-resolution encoded features with $D'_{\text{low}} < D_{\text{low}}$. Similarly to the multi-modal architecture, this one-dimensional vector is replicated spatially and concatenated with the final feature map from the U-Net-like decoder that has processed the mid-resolution group.

In all three settings, the training is done via a per-patch loss: L_{CNN} , which is a combination of weighted cross-entropy loss and dice loss. Weighted cross-entropy gives more importance to the rare class: *fire*, by increasing its loss contribution, while dice loss measures overlap: IoU, and directly optimizes for better segmentation of small or imbalanced regions. The losses are as follows:

$$L_{\text{CNN}} = L_{\text{WCE}} + L_{\text{DICE}} \quad (4)$$

$$L_{\text{WCE}} = -w_{\text{fire}} \sum_i y_i \log(\hat{y}_i) - w_{\text{no-fire}} \sum_i (1 - y_i) \log(1 - \hat{y}_i) \quad (5)$$

$$L_{\text{DICE}} = 1 - \frac{2 \sum_i y_i \hat{y}_i}{\sum_i y_i + \sum_i \hat{y}_i} \quad (6)$$

where y_i is the ground truth label for a patch (1 for *fire*, 0 for *no fire*), \hat{y}_i is the predicted probability for fire, and w_{fire} and $w_{\text{no fire}}$ are the class weights.

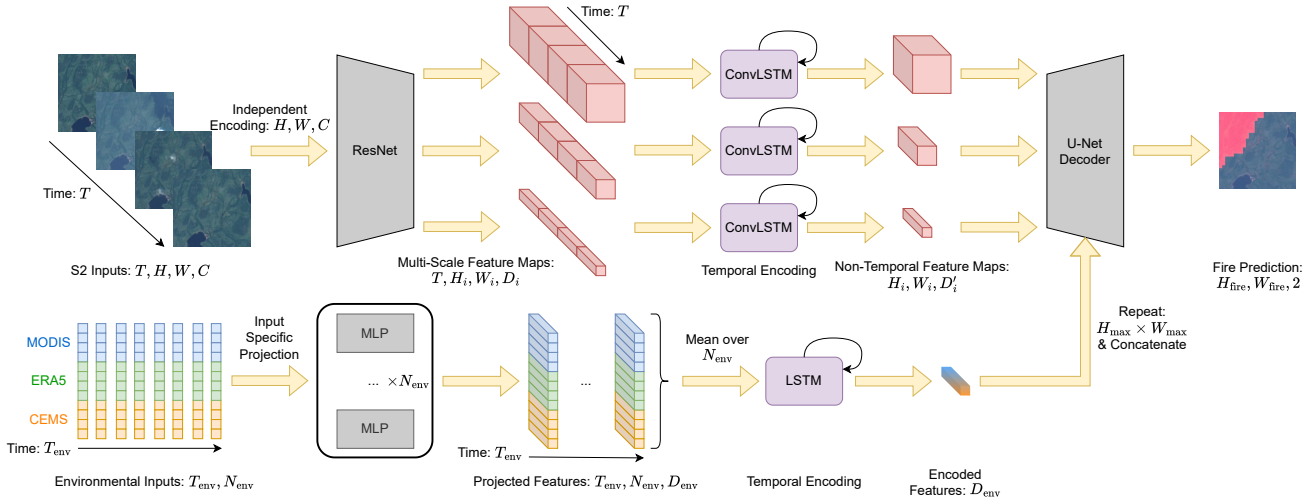


Figure 6: CNN Architecture for Wildfire Prediction in setting 3 satellite and environmental data. **Top:** Satellite image time series encoding, **Bottom:** Environmental predictors encoding.

3.2. Transformer-based Architecture

In the three settings, our ViT architectures re-use most of the components of their CNN counterparts, as shown in Figure 7, A.14, and A.15. The

main difference is the absence of multi-scale feature maps after the satellite image encoding in options **1** satellite images only and **3** satellite and environmental data, or after the mid-resolution encoding for option **2** environmental predictors only.

For a given satellite image time series $x_{1:T} = \{x_t\}_{t=1}^T$, each image $x_t \in \mathbb{R}^{H \times W \times C}$ is encoded independently by a pre-trained ViT architecture, specifically DINOv2: ViT-S (Oquab et al., 2023): $f(x_t) = \{z_t\}$, $z_t \in \mathbb{R}^{H_p \times W_p \times D_p}$, which outputs one feature map per time-step. Similarly to the CNN architecture, the encoding of all satellite images time steps is done in parallel, and the feature maps are concatenated across the temporal axis: $z_{1:T} = \{z_t\}_{t=1}^T$. As for the CNN, the temporal encoding is also done via a ConvLSTM model: $g(z_{1:T}) = s$, $s \in \mathbb{R}^{H_p \times W_p \times D_p}$. Multi-scale feature maps are not necessary for ViT due to the native high-resolution of the final output feature map: H_p and W_p . The output feature map: s , is interpolated to the label dimensions: $H_{\text{fire}} = W_{\text{fire}} = \frac{H}{10} = \frac{W}{10}$ and finally passed to the model head: a patch classification layer, to output the class probabilities: $h_{\text{ViT}}(s) = \hat{y} \in [0, 1]^{H_{\text{fire}} \times W_{\text{fire}} \times 2}$, with h_{ViT} the function representing the interpolation, and classification layer.

In the multi-modal extension **3** satellite and environmental data, the encoding of environmental inputs is identical to that of the CNN method. The final environmental encoded features $s_{\text{env}} \in \mathbb{R}^{D_{\text{env}}}$ is replicated spatially and concatenated with the final feature map s before the patch classification layer to output the class probabilities: $h(s, s_{\text{env}}) = \hat{y} \in [0, 1]^{H_{\text{fire}} \times W_{\text{fire}} \times 2}$.

For option **2** environmental predictors only, the same modifications from the satellite image time series are applied to the mid-resolution inputs; for low-resolution inputs, we use a ViT-S architecture similar to the one used for mid-resolution inputs, as it already represents the smallest available model for the DINOv2 architecture.

Contrary to the training for CNN-based architecture, the loss used here is only the dice loss as defined in Equation 6, because experimentally it led to the best results.

4. Results

This section details the key results for the benchmark models described in Section 3. CanadaFireSat covers the period 2016-2023: we train our models on years 2016-2021, while keeping 2022 for validation (Val) and 2023 for both test sets: Test and Test Hard (see Section 4.1 for details). Table 4 reports the performance of our benchmark models on CanadaFireSat.

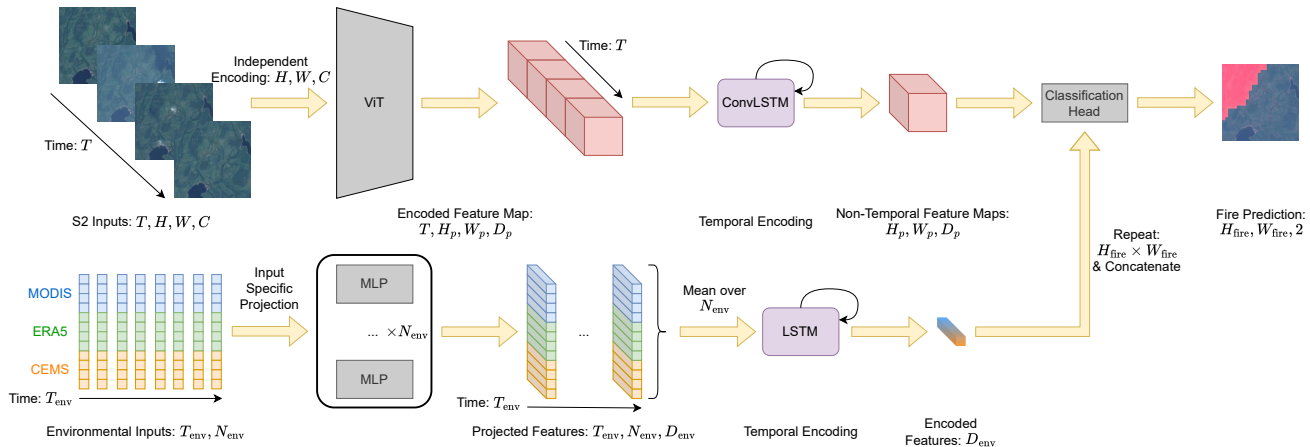


Figure 7: ViT Architecture for Wildfire Prediction in setting **3** satellite and environmental data. **Top:** Satellite image time series encoding, **Bottom:** Environmental predictors encoding.

Results are evaluated in terms of F1 score and PRAUC (Area Under the Precision-Recall Curve for the positive class *fire* only), both being robust to imbalanced datasets. The F1 score is defined as the harmonic mean between Precision (proportion of true positive pixels over pixels predicted as positive) and Recall (proportion of true positives over all actual positives):

$$F1 = 2 \times \frac{\text{Precision} \times \text{Recall}}{\text{Precision} + \text{Recall}}, \quad (7)$$

It provides information about how well the model minimizes both false negatives and false positives at a fixed threshold. PRAUC summarizes the Precision-Recall trade-off across all thresholds for the class *fire*.

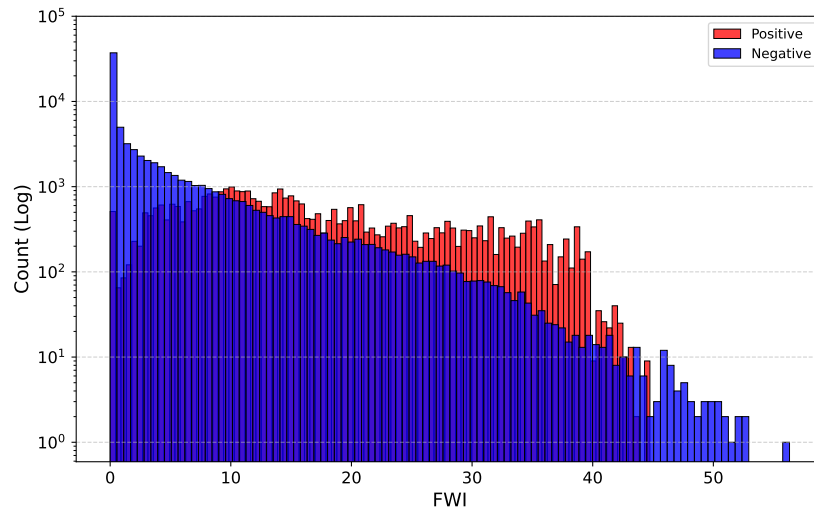
The benchmark models are tested against a baseline approach relying on the FWI. Wildfire forecasting maps are obtained from the FWI in the following way. First, for a given time step t we extract the 8-day mean FWI map at 0.25° over Canada from $t - 8$ to $t - 1$ included, and interpolate it at the target resolution of $100\text{ m} \times 100\text{ m}$. Then, the per-patch prediction is obtained by binarizing the interpolated FWI map. The optimal threshold is tuned on the validation set, referring to the year 2022: $\text{FWI}_{\text{th}} = 6$. The PRAUC is computed by scaling the FWI values with respect to the maximum value: $\text{FWI}_{\text{max}} = 50$.

4.1. Evaluation on different sets: Val, Test, and Test Hard

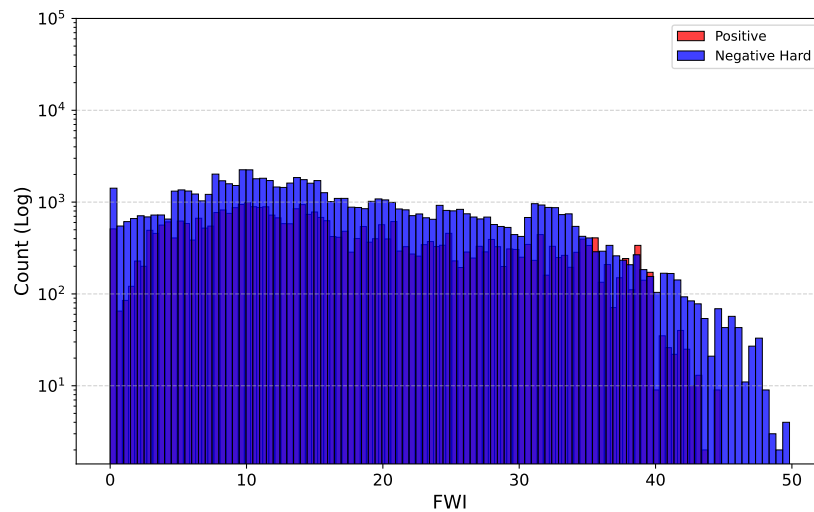
To assess the performance of the models, we rely on three different evaluation sets: Val, Test, and Test Hard. The validation (Val) and test sets (Test) represent the years 2022 and 2023 of our CanadaFireSat dataset, respectively. As such, negative examples present in these two sets follow the same sampling scheme as described in Section 2. Following a standard pipeline in machine learning, we tune the model’s hyperparameters and threshold using the F1 score on the Val set, before deploying the models on the Test set. From Table 4, a significant performance gap between Val and Test is observed for all the benchmarked models, with an increase in both PRAUC and F1 score on Test. This shift can be explained by a strong inter-annual variability between the year 2022 (Val) and the year 2023 (Test). Indeed, 2023 was a record-breaking wildfire season in Canada (Jain et al., 2024) (14.01 mha in 2023 against 1.38 in 2022, resulting in 19.6% of fire patches in the Test set compared to 11.5% in the Val set), mainly driven by warm and dry weather. Due to such extreme environmental conditions, 2023 could be considered as a simple test set when assessing the behavior of our model, with the baseline relying on the FWI only already reaching a very high F1 score of 50.3. To evaluate our models’ performance on a more challenging test set, we created a second test set named Test Hard based on an adversarial negative sampling scheme, where the FWI would be less discriminative to distinguish between the class *fire* and the class *no fire*. To make the distribution of negative samples similar to that of positives in terms of fire risk, we perform a stratified sampling of the year 2023 by extending Equation 1 to account for FWI buckets, land cover, and month of the year. Land cover is downloaded from ESA WorldCover at 10 *m* for 2020. Further analysis of the model performance threshold analysis across the three sets is shown in Appendix D.

The resulting distribution is shown in Figure 8. With this new sampling scheme, the negative sample distribution is much more similar to that of positive samples across the FWI. As a result, we can hypothesize that, in Test Hard, ignition acts as the main discriminative factor between the *fire* and *no fire* classes. As such, Test Hard represents adversarial examples for a model that learned for wildfire fuel and weather patterns. By deploying the trained networks on Test Hard, we can assess their performance for modeling ignition, a complex triggering factor that is not taken into account by the FWI, but whose pattern can be implicitly learned by deep models from the training data. For this reason, the performance of our trained models for high-resolution wildfire forecasting on Test Hard can be considered as a

lower bound for such an extreme wildfire season. Further details about the distribution of samples across land-cover classes are provided in Figure D.17.



(a) FWI distribution in log-scale for the Test set across positive and negative samples.



(b) FWI distribution in log-scale for the Test Hard set across positive and negative samples.

Figure 8: Comparison of the FWI distribution in log-scale across the Test and Test Hard sets for both positive and negative samples.

4.2. Performance Analysis

We evaluate the performance of the two different architectures, CNN and ViT, across three different settings described in Section 3: **1** satellite images only, **2** environmental predictors only, and **3** satellite and environmental data. The results are reported in Table 4.

Encoder	Modality	Params (M)	Val		Test		Test Hard		Avg	
			PRAUC	F1	PRAUC	F1	PRAUC	F1	PRAUC	F1
ResNet-50	SITS Only	52.2	<u>45.2</u>	<u>49.3</u>	<u>53.3</u>	<u>58.9</u>	<u>26.3</u>	<u>36.7</u>	<u>41.6</u>	<u>48.3</u>
	ENV Only	97.5	41.6	46.7	49.9	53.5	24.5	33.1	38.7	44.4
	Multi-Modal	52.2	46.1	51.1	57.0	60.3	27.1	37.4	43.4	49.6
ViT-S	SITS Only	36.5	45.2	50.6	<u>51.2</u>	51.9	25.7	33.8	<u>40.7</u>	45.2
	ENV Only	54.8	34.8	45.7	49.2	59.9	21.2	<u>35.1</u>	35.1	<u>46.9</u>
	Multi-Modal	37.7	<u>43.9</u>	<u>50.0</u>	56.3	<u>59.2</u>	<u>25.1</u>	36.6	41.8	48.6
Baseline (FWI)	ENV Only	-	20.0	32.7	43.1	50.3	21.1	32.7	28.1	38.6

Table 4: Performance comparison of different model settings.

Across the three evaluation sets (last column of Table 4), both ResNet-50 and ViT-S trained on **3** satellite and environmental data reach the highest performance, with +15% PRAUC and +11% F1 score for the CNN, compared to the FWI baseline. For both the CNN and ViT architectures, relying on multi-modal inputs shows an improvement over models trained on **1** satellite images only or **2** environmental predictors only. While individually **1** satellite images only and **2** environmental predictors only are already highly discriminative, the multi-modal setting **3** satellite and environmental data remains the most accurate forecaster with an average gain of +1.8% in PRAUC and +1.3% in F1 score for CNN-based models and +1.1% in PRAUC and +1.7% in F1 score for the ViT. We further discuss the role of satellite image time series and environmental predictors in Section 5.1. On the original Test set, the better performance of all models (compared to the Val set) can be explained by fire patterns likely being more easily distinguishable due to the extreme fire season, a behavior also observed in the FWI baseline. Nonetheless, our best performing CNN model relying on **3** satellite and environmental data still outperforms the FWI baseline, on the Test set by +13.9% (PRAUC) and by +10% (F1 score). The drop in performance of all models on the Test Hard set demonstrates the impact of the sampling strategy and the necessity of such an evaluation set to provide a lower bound of performance, as the models were not trained on such adversarial negative samples. When it comes

to the comparison between ResNet-50 and ViT-S trained on **3** satellite and environmental data, the former shows to perform best in terms of F1 score across all sets. However, differences remain small, and both architectures seem valid solutions for wildfire forecasting.

The performances of the different models in setting **3** satellite and environmental data are studied in Figure 9 for increasing FWI values. We first focus on the False Positive Rate, defined as $FPR = \frac{FP}{FP+TN}$. As expected, we can observe in Figure 9a a positive correlation between the FPR and the FWI. Indeed, negative samples associated with a higher FWI show similar fire danger conditions to positive samples, and are thus much more difficult to discriminate, with ignition becoming the main triggering factor for samples with $FWI > 20$. Then, we study in Figure 9b the variations of the weighted F1 score, defined as $\hat{F1} = \frac{F1 - F1_{pos}}{1 - F1_{pos}}$. This second index tells how good the model is compared to a naive predictor: $F1_{pos}$, assigning the class *fire* to all samples. We note a negative correlation between $\hat{F1}$ and the FWI: as the FWI increases, there is approximately no difference between our benchmark models and the naive predictor. Such behavior is not surprising as it is more likely for a sample associated to a high FWI to belong to the class *fire*, as confirmed by the increase in percentage of positive samples with higher FWI (from 13% at $FWI \in [0, 5]$ to 77% at $FWI \in [20, 30]$). We can conclude that the improved performance of our model w.r.t. the FWI baseline reported in Table 4 is due to a better prediction of wildfire occurrence at lower FWIs, as the task becomes trivial for $FWI > 20$ due to data imbalance.

We also study the results of ResNet-50 and ViT-S trained on **3** satellite and environmental data across the most common land cover classes in CanadaFireSat. Our models struggle the most on the classes *wetland* and *cropland*. Indeed, fire patterns in these two land cover types differ from those observed in the majority of wildfires, affecting forest areas. In particular, peatland fires in Canada can occur under the ground in wet areas, or even under the snow layer. Such fires are difficult to observe through the predictors considered in the proposed CanadaFireSat, and would require *ad-hoc* modeling due to the specificities of such ecosystems. Low scores are also observed for cropland fires, which also present unique fire patterns, as the ignition is often human-induced and driven by a specific need for agricultural practices.

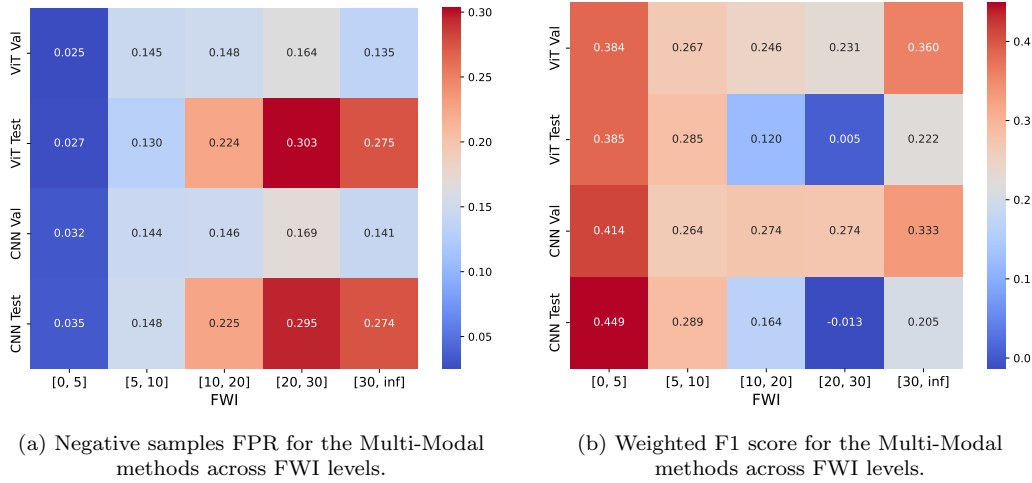


Figure 9: **3** satellite and environmental data models’ performance across different FWI value groups.

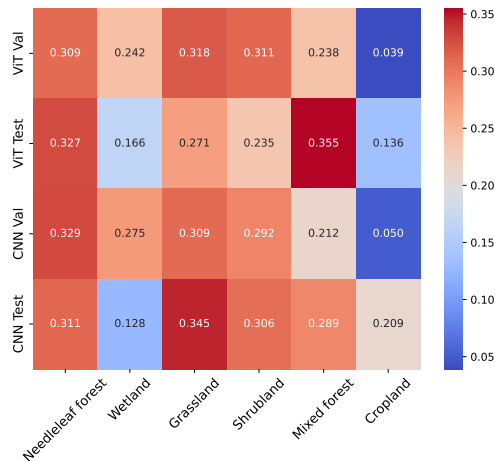


Figure 10: **3** satellite and environmental data models’ performance across the main land cover classes.

4.3. Deployment at Scale: Case Study

CanadaFireSat enables training deep models for high-resolution wildfire forecasting. As a result, our dataset makes it possible to deploy models capable of monitoring large regions at high-resolution. In this section, we demonstrate on a real use case how a model trained on our CanadaFireSat dataset could be deployed at a scale useful for wildfire management teams.

We chose a large wildfire that occurred in Québec on 2023/07/05 as a case study, illustrated in Figure 11. The first row displays the RGB composite of the region of interest of size $14\text{km} \times 26\text{km}$ acquired by Sentinel-2 right before the wildfire starts on 2023/06/28. The fire scar polygons from NBAC are shown on the second row. The third row shows the predictions of the CNN model trained in the multi-modal setting **③ satellite and environmental data**, on the positive samples overlapping with the considered ROI. The predictions follow the same pattern as the actual wildfire, despite slightly overestimating its extent, as it can be seen on both sides of the Sentinel-2 tile. This case study showcases the potential of CanadaFireSat to enable the deployment of models capable of monitoring large regions at high-resolution (i.e., Sentinel-2 spatial resolution).

5. Discussion

5.1. High-resolution Wildfire Forecasting via Multi-modal Learning

As previously demonstrated in (Pelletier et al., 2023; Chowdhury and Hassan, 2015; Yang et al., 2021), multi-spectral multi-temporal satellite data can be a valuable predictor for wildfire forecasting. Indeed, several spectral indexes discriminative for wildfire forecasting can be extracted from Sentinel-2: normalized difference vegetation index (NDVI), normalized difference water index (NDWI), tasseled cap wetness, and channel histograms. The results reported in Table 4 demonstrate the potential of multi-spectral temporal satellite data for high-resolution wildfire forecasting (setting **① satellite images only**). While hydrometeorological data (setting **② environmental predictors only**) are commonly used in global and continental wildfire forecasting models, they can be complemented by satellite data to improve strongly both the spatial resolution and the accuracy of the prediction (setting **③ satellite and environmental data**).

5.2. Importance of Negative Sampling for Training and Evaluation

Numerous wildfire forecasting benchmarks require sampling the negative (non-fire) samples due to extreme imbalance and computational constraints. A common strategy is to focus on samples that burned once across the period studied (Prapas et al., 2022; Bakke et al., 2023; Prapas et al., 2023). In CanadaFireSat, we opt for a different strategy as we sample negative examples for each Canadian province uniformly across their yearly fire driver patterns (FWI values). By sampling the training, validation, and test sets

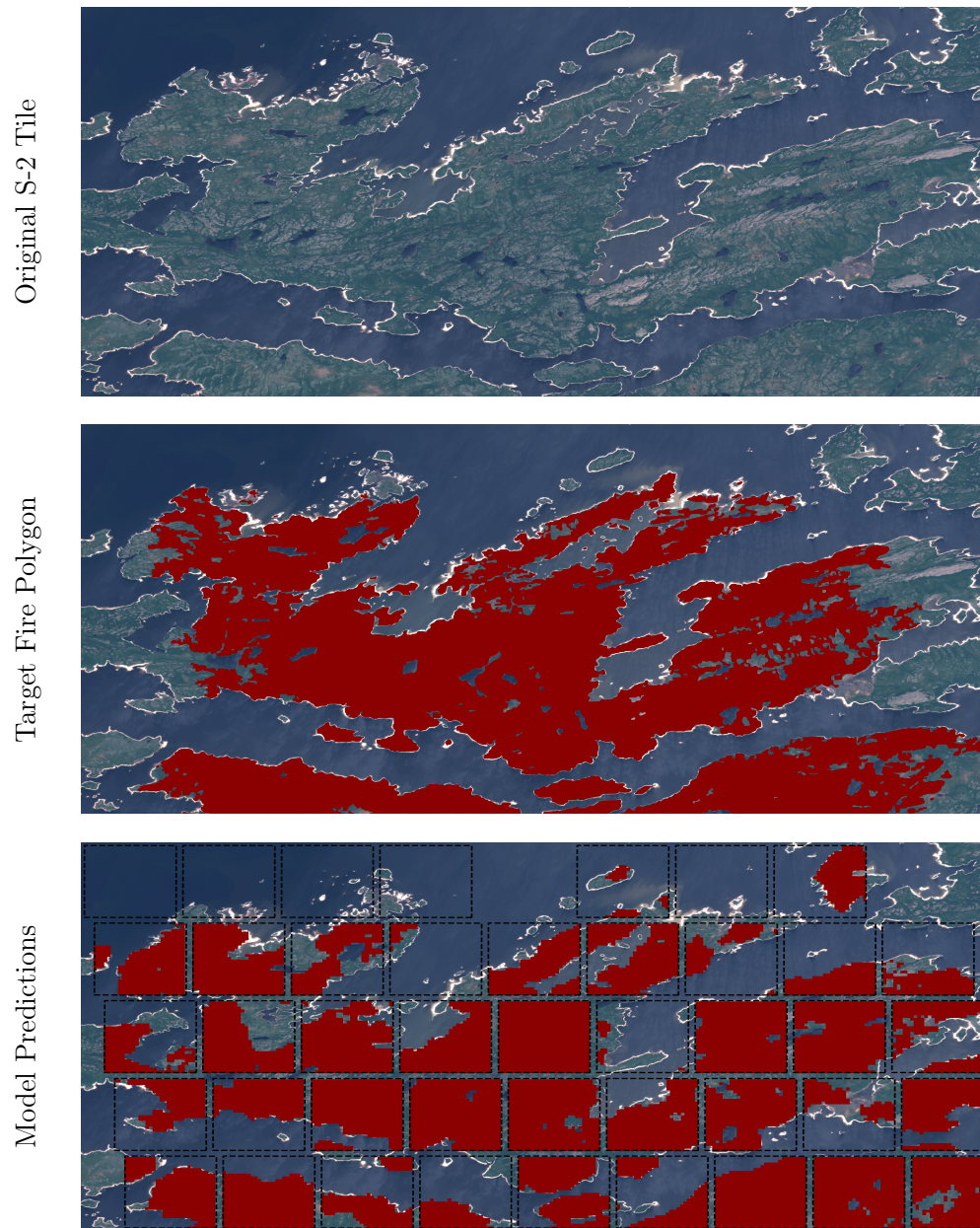


Figure 11: **Row 1** Sentinel-2 tile from 2023/06/28 of size $14 \text{ km} \times 26 \text{ km}$ before a large wildfire in Québec. **Row 2** Fire polygons for the large wildfire on 2023/07/05 over the same tile. **Row 3** Binary model predictions (in **red**) over the $2.64 \text{ km} \times 2.64 \text{ km}$ center-cropped positive samples outlined in **black**.

in this way, we aim to train and evaluate our models on a subset representative of the conditions encountered in the entire Canada. Nonetheless, as the yearly fire patterns vary, the distribution of negatives w.r.t. the FWI changes over the years, in turn affecting models’ performance. This motivated the creation of a second test set to understand the impact of sampling on the models’ performance: Test Hard, sampled differently by aiming to replicate as close as possible relevant fire drivers from the positive set. We consider Test Hard as a lower bound for our model performance, since the main predictors for differentiating positive from negative patches are linked to ignition, a complex phenomenon difficult to model (Chen et al., 2021; Calef et al., 2008). Indeed, despite identical hydrometeorological conditions, a random ignition caused by humans or lightning is still necessary to cause a wildfire. Theoretically, wildfire forecasting could be framed as a positive unlabeled learning task (Bekker and Davis, 2020) to explicitly model the differences between fire conditions and ignition in wildfire forecasting. Examples of positive unlabeled tasks can be found in several environmental and ecological applications, like species distribution modeling (Zbinden et al., 2024) and phenology event detection (Fasihi et al., 2025). Fine-tuning our multi-modal models on data such as Test Hard or enhancing our set of predictors with proxies of ignition probability (e.g, proximity to human settlements, or lightning probability) are relevant directions for improving our models towards accounting for ignition probability.

5.3. Modeling Wildfires in the Boreal Ecosystem

As initially stated in Section 1, one of our main motivations is the rise of wildfires in the boreal ecosystem and the risks this represents for its local communities. To cover the areas of interest and to evaluate the broader impact of wildfires on global climate, we created our benchmark CanadaFireSat so that it covers the entirety of Canada, including all its agricultural lands, urban areas, and other ecosystems such as the temperate forest in British Columbia. To study the behavior of trained models on the boreal ecosystem, it is possible to constrain the analysis on the main land cover classes of the boreal ecosystem (needleleaf forest and wetlands). With our benchmark models trained on CanadaFireSat, we observe an important difference of performance between those two land cover classes: with Multi-Modal CNN and ViT performing respectively +11.9% and +11.4% better on needleleaf forest compare to wetlands in terms of weighted F1 score on Val and Test. Indeed, wetland wildfires are a unique phenomenon compared to forest wildfires as

they depend much more on soil-related predictors and can burn underground for a long period. As a consequence, they are sometimes undetectable for optical remote sensing satellites. In particular, peatland wildfires that emit large amounts of CO₂ and mercury (Fraser et al., 2018; Kohlenberg et al., 2018) are commonly studied independently from forest fires (Pelletier et al., 2023; Bali et al., 2021). Extending CanadaFireSat so that it includes data acquired from radar remote sensing satellites (for instance, Sentinel-1 images) could help to better model the surface soil conditions for wetlands and bridge the gap in performance across the boreal ecosystem.

5.4. Operationalization of the Model

Deploying models trained with CanadaFireSat over the entirety of Canada would require densely sampling the country with Sentinel-2 image time series, resulting in a huge amount of data to be processed. Indeed, the proposed dataset is aimed at modeling wildfire patterns at a moderate scale, but at high-resolution, and can be coupled with coarser resolution approaches (Prapas et al., 2022; Bali et al., 2021) to identify areas of interest and then apply our model to map such areas more precisely. Such coupling would allow wildfire management experts to target specific areas at risk for fine-grained wildfire forecasting or focus on areas that require more surveillance due to their proximity to local communities or due to their ecological and environmental interest. Learning models directly capable of multi-scale prediction is an interesting future research direction to deploy high-resolution wildfire forecasting at scale. Such a model would exploit hierarchical learning approaches developed in computer vision for semantic segmentation (Li et al., 2022; Atigh et al., 2022).

5.5. Limitations and Future Work

As mentioned in Section 5.2, the main limitation of methods trained on CanadaFireSat is the difficulty of modeling the ignition component in wildfires due to its inherent stochasticity. Weather data from ERA5 can provide information on the risk of lightning, nonetheless, explicitly adding lightning probability (Geng et al., 2019) as a predictor, as well as other proxies for human ignition, like the proximity to human settlement, could help the trained models to characterize ignition better.

Multi-task learning (Zhang and Yang, 2021) can also be leveraged to develop a model capable of forecasting wildfires at multiple scales. One could leverage different forecasting heads at multiple resolutions: 10 km, 1 km, 100

m. This could help alleviate memory size constraints when high-resolution forecasts are deemed unnecessary and help providing consistent predictions across scales. Indeed, hierarchical learning (Li et al., 2022) can also be linked to multi-scale wildfire forecasting, as one can build a hierarchical structure across labels at different resolutions.

Moreover, one could investigate the potential of geolocation embeddings such as SatCLIP (Klemmer et al., 2023) or GeoCLIP (Vivanco Cepeda et al., 2023) to represent high-resolution non-dynamic satellite information combined with non-spatial, but temporal dynamics from Sentinel-2 (Pelletier et al., 2023), as a way to factorize spatial and temporal components in satellite data and limit memory consumption.

Another line of improvement would be relying on pre-trained foundation models for Earth observation. For our Multi-Modal architectures, we leverage image encoders pre-trained on natural images such as ImageNet or via DINOv2, which are very different from multi-spectral satellite images. With the drastic increase in availability of Earth observation data, several models are being proposed to learn in an unsupervised way generalizable representations from this data (Cong et al., 2022; Jakubik et al., 2023; Hong et al., 2024; Astruc et al., 2024). Those models are mainly driven by the concept of masked auto-encoders (He et al., 2022) and contrastive learning (Chen et al., 2020; He et al., 2020). One could study the potential of those foundation models on high-resolution wildfire forecasting by fine-tuning them on CanadaFireSat.

Finally, the increased complexity of models raises concerns regarding their interpretability and the possibility of understanding the role of the input variables in the final predictions. Several approaches exist to provide interpretations of black box wildfire forecasting models via feature attributions (Sundararajan et al., 2017; Selvaraju et al., 2017) or ranking (Lundberg and Lee, 2017), or even to directly build interpretable wildfire forecasting model architectures (Koh et al., 2020; Chen et al., 2019) via dense prediction architecture (Sacha et al., 2023; Porta et al., 2025a). However, those methods need adaptation to accommodate multi-modal (Ekim and Schmitt, 2023; Wang et al., 2023) or multi-temporal data (Turbé et al., 2023; Gee et al., 2019; Ghosal and Abbasi-Asl, 2021). They are also often not directly applicable to Earth observation data (Porta et al., 2025b) due to strong implicit bias for natural images (Chen et al., 2019). This gap remains unfulfilled, and future works should explore interpretable methods specifically tailored to Earth observations problem.

6. Conclusion

In this paper, we introduced CanadaFireSat, a comprehensive benchmark dataset for high-resolution wildfire forecasting over Canada from 2016 to 2023. CanadaFireSat was constructed to support multiple settings for model training: **①** satellite images only, **②** environmental predictors only, and **③** satellite and environmental data. We demonstrated experimentally the potential of multi-modal learning for high-resolution wildfire forecasting on CanadaFireSat across two architectures: ResNet and ViT. Moreover, our experiments showed the importance of negative sampling in the evaluation of wildfire forecasting models. CanadaFireSat aims to accelerate research towards high-resolution monitoring of at-risk regions of interest to support wildfire management teams who are tasked with monitoring and protecting vast areas, such as the boreal ecosystem covering much of Canada. Results from this work demonstrate the feasibility of constructing future datasets like CanadaFireSat for other fire-prone landscapes, like the Pan-Arctic, Pan-boreal, and grassland and forest ecosystems of the Tropics. We hope this dataset and benchmark will foster research in this direction. To facilitate that, all codes, models, and CanadaFireSat are made publicly available on GitHub and HuggingFace.

Appendix A. Model Architectures

In this section, we illustrate the architectures used in the settings **1** satellite images only and **3** satellite and environmental data for the CNN-based models: Figure A.12 and A.13. We then show those used in the Transformer-based models: Figure A.14 and A.15.

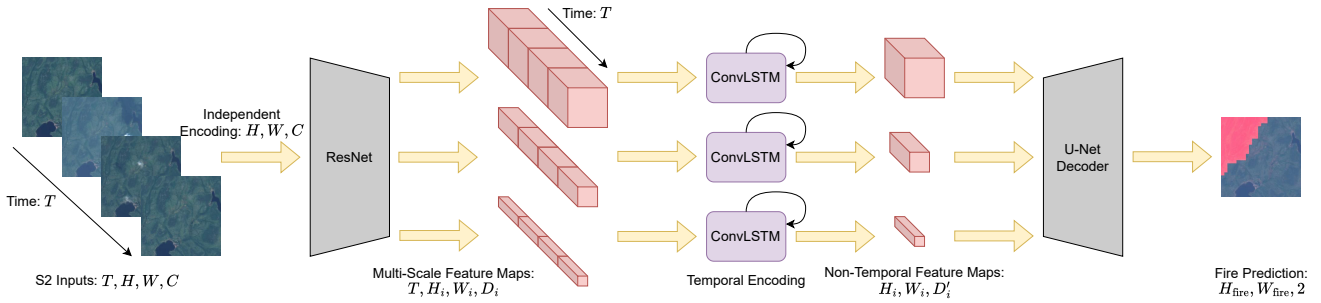


Figure A.12: CNN Architecture for Wildfire Prediction used for setting **1** satellite images only.

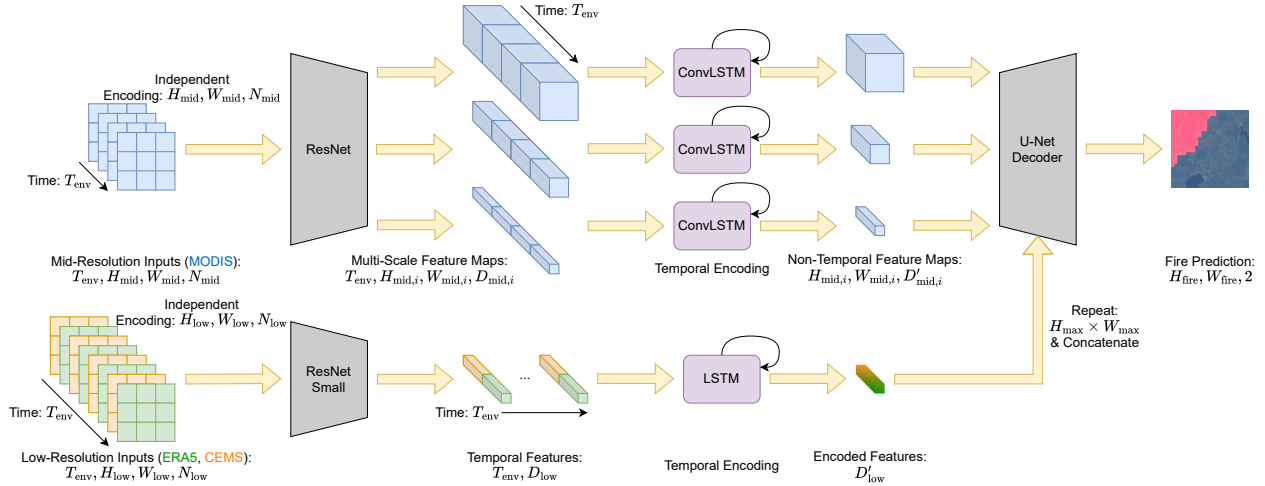


Figure A.13: CNN Architecture for Wildfire Prediction used for Setting **2** environmental predictors only.

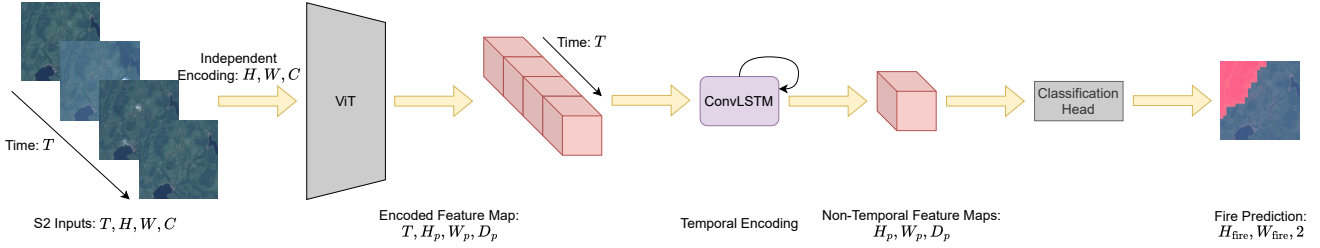


Figure A.14: ViT Architecture for Wildfire Prediction used for Setting ❶ satellite images only.

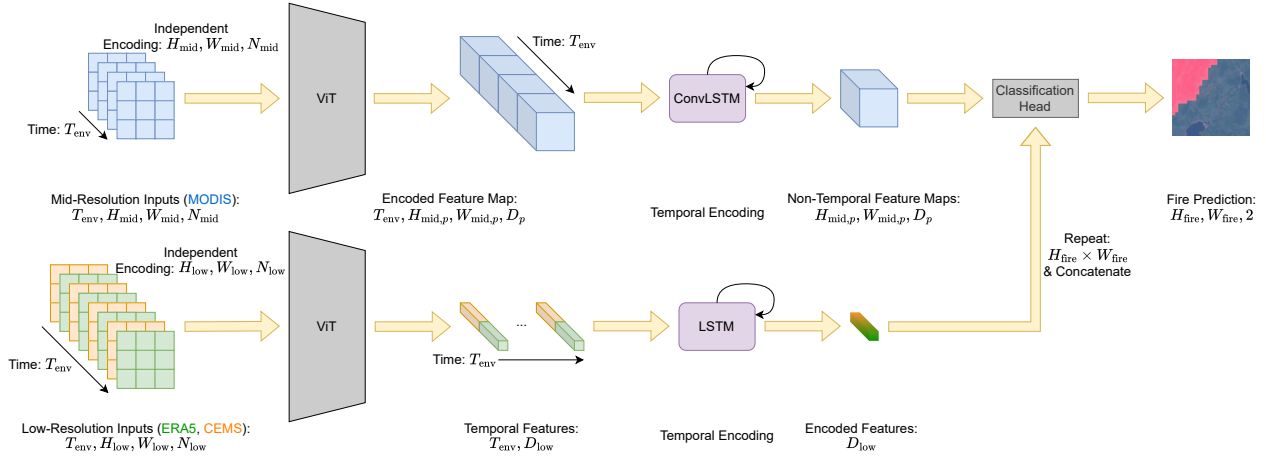


Figure A.15: ViT Architecture for Wildfire Prediction used for Setting ❷ environmental predictors only.

Appendix B. Experimental Setup:

Appendix B.1. CNN Architecture Parameters

As mentioned in Section 3.1, satellite image time series encoding is done via a ResNet-50 backbone pre-trained on ImageNet. During training, the inputs are of size $T = 5$, $C = 14$, and $H = W = 240$ leading to a target resolution $H_{\text{fire}} = W_{\text{fire}} = 24$. During testing, we compute the prediction on the whole sample of size $H = W = 260$ with the same T and C , leading to $H_{\text{fire}} = W_{\text{fire}} = 26$. We extract the model's last three feature maps of channel dimensions: 512, 1024, and 2048. Those feature maps pass through three independent ConvLSTM models, each one with kernel size 3×3 and only one layer. The ConvLSTM models output feature maps of dimensions: 64,

128, and 256, which are then passed to a U-Net-like decoder and interpolated to the target size.

This model is extended to multi-modal inputs of dimensions $N_{\text{env}} = 15$, including the day of the year, and $T_{\text{env}} = 8$, as we leverage the whole time series for those inputs. This data is projected to a high-dimensional space of size $D_{\text{env}} = 64$ and passed to an LSTM with one layer. The selected environmental predictors are the following: Total Precipitation Sum: 8-day Mean, Skin Temperature: 8-day Mean, Temperature (2m): 8-day Mean, Volumetric Soil Water Layer 1: 8-day Mean, Wind Speed (10m): 8-day Mean, Relative Humidity: 8-day Mean, Vapor Pressure Deficit: 8-day Mean, LST Day (1km): 8-day Mean, NDVI, EVI, FPAR, LAI, Drought Code: 8-day Mean, Fire Weather Index: 8-day Mean.

The model using only environmental predictors leverages inputs of dimension $H_{\text{mid}} = W_{\text{mid}} = 32$ for mid-resolution data: MODIS, and $H_{\text{low}} = W_{\text{low}} = 32$ for low-resolution data: ERA5, CEMS. MODIS data at 1 km: LST Day is interpolated to 500m to align with the rest of the MODIS inputs. Similarly, for the CEMS data: Fire Weather Index, and Drought Code, at 0.25° , is interpolated to 11.1 km to align with ERA5-Land. We leverage the same set of environmental predictors as in the multi-modal setting, split into the two resolution groups. The temporal dimension of those inputs is $T_{\text{env}} = 8$, the number of mid-resolution predictors is $N_{\text{mid}} = 6$ including the day of the year, and the number of low-resolution predictors is $N_{\text{low}} = 10$ including the day of the year (one more dimension than N_{env} as we include the day of the year twice). As mentioned in Section 3.1, for the mid-resolution group we leverage $N_S = 5$ multi-scale feature maps of dimensions: 64, 256, 512, 1024, and 2048, for the mid-resolution data. The last feature map of channel dimension 2048 is one-dimensional and is passed as such to an LSTM network for the temporal encoding. For the other four, we use independent ConvLSTM models. Those temporal encoders output feature maps of dimensions: 64, 128, 256, 512, and 1024, which are passed to a U-Net-like decoder and interpolated to the target size. The low-resolution inputs are encoded via a smaller network: ResNet-18, which outputs feature maps of channel dimension $D_{\text{low}} = 512$, encoded temporally with a LSTM with of one layer to a dimension $D'_{\text{low}} = 64$, matching the channel dimension of the last feature map of the U-Net decoder. Both ResNet encoders are pre-trained on ImageNet. As for the other settings, the training is done with a target resolution of size $H_{\text{fire}} = W_{\text{fire}} = 24$, and at test time the target resolution is $H_{\text{fire}} = W_{\text{fire}} = 26$.

Appendix B.2. ViT Architecture Parameters

In the case of the ViT architecture, the satellite image time series encoding is done via the DINOv2 ViT-S architecture. The input channel and temporal dimensions are the same as for the CNN architecture: $T = 5$, and $C = 14$. However, since the patch size of the ViT encoder is 14, we used as input spatial dimensions a direct multiple: $H = W = 252$ during training. As a consequence, during training $H_{\text{fire}} = W_{\text{fire}} = 25$. At test time, input and target dimensions are the same as for the CNN use case. To reduce overfitting issues, we used the LORA method (Hu et al., 2022) to fine-tune the ViT model with rank $r = 32$, $\alpha = 32$, and dropout $d_{\text{LORA}} = 0.1$. The channel dimension of the encoded feature map is $D_p = 384$, which is maintained after temporal encoding via ConvLSTM with kernel size 3×3 .

The model extension for multi-modal data is done similarly to the CNN case with $D_{\text{env}} = 384$. This is to match the channel dimension of the final feature map. The same set of environmental predictors is used for this setting as for the CNN architecture above.

For the environmental-only architecture, the input and target spatial dimensions and processing are identical to the CNN use case. The temporal dimension differs as we use $T_{\text{env}} = 5$ for data augmentation. Both mid-resolution and low-resolution ViT-S encoders are randomly initialized and therefore do not use the LORA method for fine-tuning. In both encoders for the position embedding, attention, and projection, we use a dropout $d_{\text{env}} = 0.2$ and a stochastic depth rate of $d_{\text{depth}} = 0.1$. For mid-resolution inputs, the patch size is 2, and for low-resolution inputs, the patch size is 8. The temporal encoding of the mid-resolution feature map is identical to the one used for the satellite image time series, and the temporal encoding of the low-resolution data is done through a one-layer LSTM with both input and output channel dimensions $D_{\text{low}} = 384$.

Appendix B.3. CNN Training Parameters

The CNN models are trained using the combined weighted cross-entropy and dice loss. The positive class (fire) weight is 0.87 and the negative class (no fire) is 0.13, found experimentally. Training is run over 20 epochs with a batch size of 24 samples on a NVIDIA GeForce RTX 3080 Ti GPU. The scheduler for the learning rate follows a 2-epoch warm-up from the starting learning rate of $1e^{-7}$ to the base learning rate of $5e^{-6}$. Then the learning rate follows a cosine annealing of one cycle to the minimum learning rate of $1e^{-7}$ over the rest of the epochs. The optimizer used is ADAMW with a weight decay

of 0.01. During training, the augmentation pipeline first randomly crops the satellite input images to the training resolution, then resizes the images with a scale $s \in [0.9, 1]$. The images are randomly flipped horizontally and vertically, and Gaussian noise injection is done with variance $\sigma^2 \in [0.01, 0.1]$. Finally, we randomly sample the satellite image time series to extract $T = 5$ images (or pad when necessary). At test time, we center-crop the images to the required resolution and select the last $T = 5$ samples. For the multi-modal training, the non-spatial environmental data is not augmented, while for the environment-only architecture, we apply random horizontal and vertical flipping and Gaussian noise injection, similarly to the satellite image time series. The missing values in the environmental predictors, mainly caused by the NDVI and EVI as they are 16-day composites, are replaced during training with the value 0.0.

Appendix B.4. ViT Training Parameters

Most of the ViT training parameters are the same as for the CNN models, except for the batch, which, despite also being 24, is accumulated across two steps of 12 for the ViT models. Moreover, during the training of the environmental-only use case, as we select $T_{\text{env}} = 5$ time steps, it is also necessary to randomly sample across the total 8 available samples. Finally, at test time across all modalities, we use the native temporal length for each sample, 8 for the environmental data and a variable length for the satellite image time series. The processing of the missing values for the environmental predictors is the same as for the CNN-based architecture.

Appendix C. Ablation Study of the Impact of Satellite Image Time Series

In Table C.5, we analyze the performance of the multi-modal models in setting **3 satellite and environmental data** with respect to the usage of time series. We compare our full multi-modal model using satellite image time series against a version using only the most recent image available before the prediction. In practice, for the CNN-based model, this impacts the number of parameters in the U-Net decoder as $D_i > D'_i$. Table C.5 shows the impact of SITS on model performance in setting **3 satellite and environmental data**, where, regardless of the architectures, the model performs best when presented with SITS rather than a single Sentinel-2 tile. As a consequence,

we can hypothesize that dynamic factors directly linked to wildfire can be learned by the model from the temporal dimension of Sentinel-2.

Encoder	SITS	PRAUC	F1
ResNet-50	✗	42.4	48.3
ResNet-50	✓	46.1	51.1
ViT-S	✗	38.2	47.4
ViT-S	✓	43.9	50.0

Table C.5: Ablation study of SITS impact on the validation set performance.

Appendix D. Test Hard Analysis

Figure D.16 demonstrates the domain shift between the Val and the Test set, as the evolution of the F1 score with the probability threshold is centered around 0.5 for the Val set, presenting a normal behavior while being shifted towards a smaller threshold value for the Test set. As a consequence, the metrics in Table 4 might overestimate the model performance on the test set due to the extreme fire patterns during this year. For this purpose, we constructed the adversarial set named Test Hard for the year 2023 as described in Section 4. Figure D.16 also shows the delta in performance between Test and Test Hard and the centering of the maximum value for Test Hard closer to the 0.5 threshold, representing a better alignment with the model behavior on the Val set.

Figure D.17 presents the change in land cover distribution for the negative samples between the two sets: Test and Test Hard, with respect to the positive samples. The stratification sampling, done in Test Hard, aligns better the categorical distributions for the negative and positive populations.

Appendix E. Deployment at Scale: Second Case Study

In Figure E.18, we present another case study for our CNN-based model in setting **3 satellite and environmental data**. This example presents a large wildfire in British Columbia occurring on the 2023/07/01, displayed over an RGB composite of a Sentinel-2 image of $16 \text{ km} \times 22 \text{ km}$. Comparing our predictions with the positive samples covering this region of interest, we

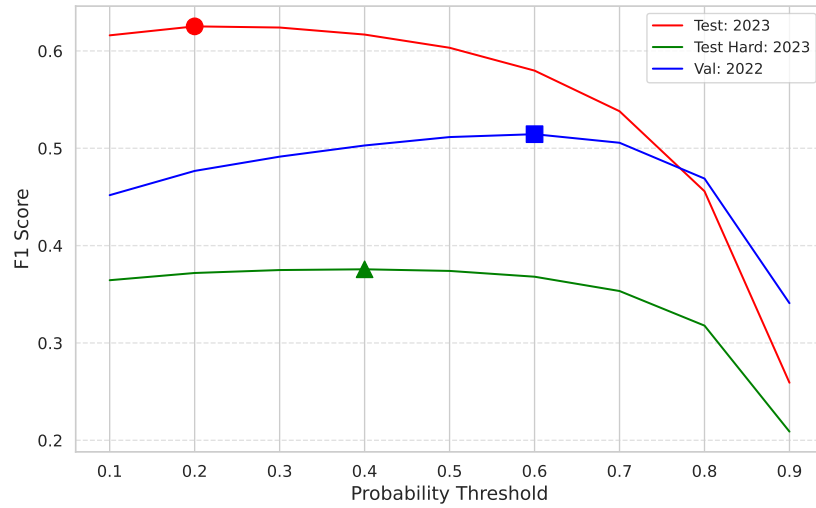
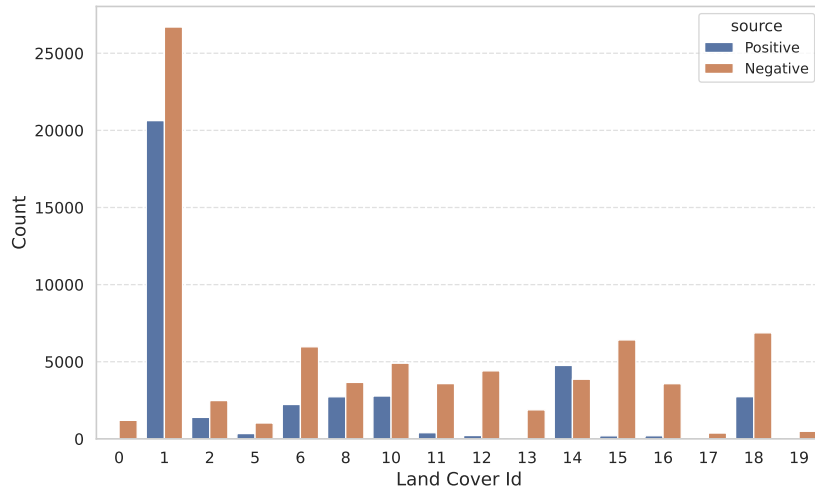
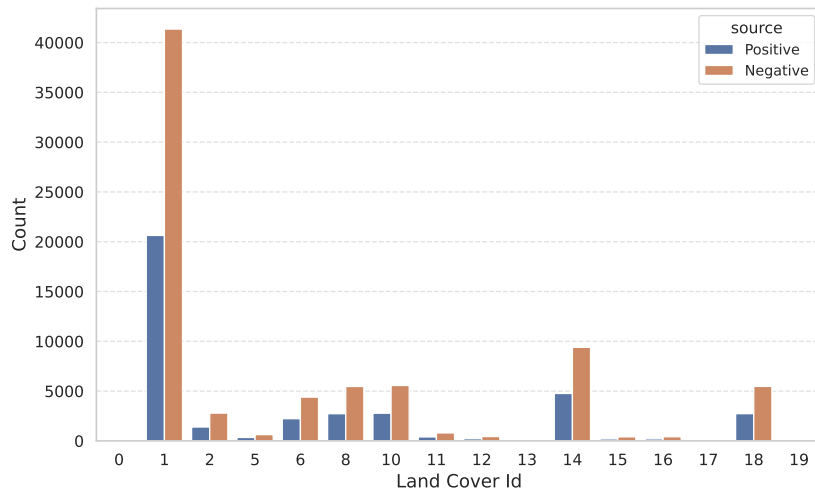


Figure D.16: Analysis of the F1 score performance as a function of the probability threshold across all evaluation sets. The circle, square, and triangle represent the maximum value for each set.

observe how well the model delineates the urban interface on the left side of the wildfire and the rough approximation of its boundaries on the right side of the fire. However, we can also see at the top of the Sentinel-2 image that the model overestimates the wildfire extent, similarly to what we observed in 11.



(a) Land cover distribution for the Test set across positive and negative samples.



(b) Land cover distribution for the Test Hard set across positive and negative samples.

Figure D.17: Comparison of the land cover distribution across the Test and Test Hard sets for the positive and negative samples.

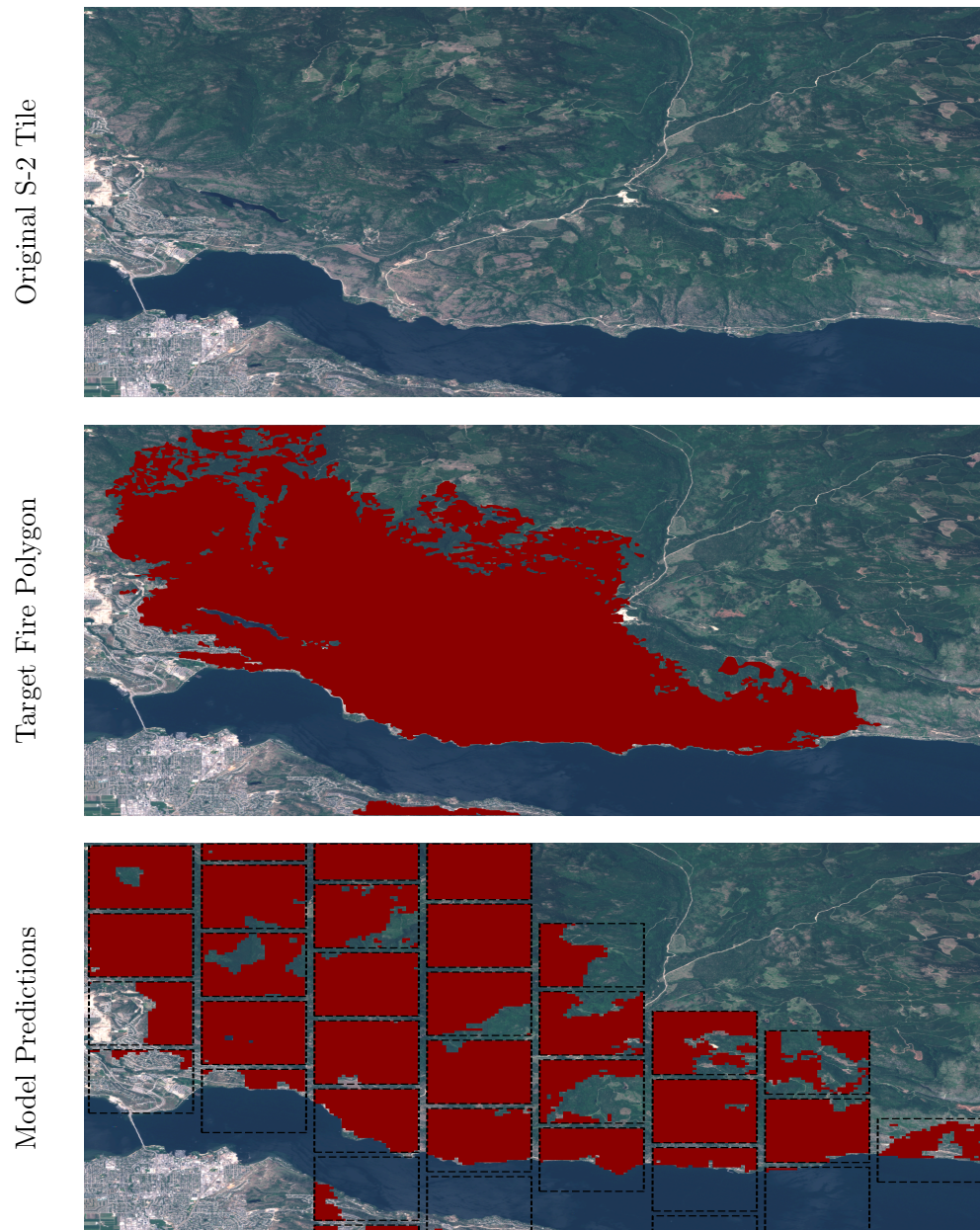


Figure E.18: **Row 1** Sentinel-2 tile from 2023/06/06 of size $16\text{ km} \times 22\text{ km}$ before a large wildfire in British Columbia. **Row 2** Fire polygons for the large wildfire on 2023/07/01 over the same tile. **Row 3** Binary model predictions (in **red**) over the $2.64\text{ km} \times 2.64\text{ km}$ center-cropped positive samples in **black**.

References

- de Almeida Pereira, G.H., Fusioka, A.M., Nassu, B.T., Minetto, R., 2021. Active fire detection in landsat-8 imagery: A large-scale dataset and a deep-learning study. *ISPRS Journal of Photogrammetry and Remote Sensing* 178, 171–186.
- Astruc, G., Gonthier, N., Mallet, C., Landrieu, L., 2024. Anysat: An earth observation model for any resolutions, scales, and modalities. *arXiv preprint arXiv:2412.14123* .
- Atigh, M.G., Schoep, J., Acar, E., Van Noord, N., Mettes, P., 2022. Hyperbolic image segmentation, in: *Proceedings of the IEEE/CVF conference on computer vision and pattern recognition*, pp. 4453–4462.
- Bakke, S.J., Wanders, N., Van Der Wiel, K., Tallaksen, L.M., 2023. A data-driven model for fennoscandian wildfire danger. *Natural hazards and earth system sciences* 23, 65–89.
- Bali, S., Zheng, S., Gupta, A., Wu, Y., Chen, B., Chowdhury, A., Khim, J., 2021. Prediction of boreal peatland fires in canada using spatio-temporal methods, in: *Climate Change AI. ICML 2021 Workshop on Tackling Climate Change with Machine Learning. Climate Change AI*. URL: <https://www.climatechange.ai/papers/icml2021/12> (visited on 01/19/2023).
- Barnosky, A.D., Matzke, N., Tomiya, S., Wogan, G.O., Swartz, B., Quental, T.B., Marshall, C., McGuire, J.L., Lindsey, E.L., Maguire, K.C., et al., 2011. Has the earth’s sixth mass extinction already arrived? *Nature* 471, 51–57.
- Bates, B.C., Dowdy, A.J., McCaw, L., 2021. A bayesian approach to exploring the influence of climate variability modes on fire weather conditions and lightning-ignited wildfires. *Climate Dynamics* 57, 1207–1225.
- Bekker, J., Davis, J., 2020. Learning from positive and unlabeled data: A survey. *Machine Learning* 109, 719–760.
- Bourgeau-Chavez, L.L., Graham, J.A., Vander Bilt, D.J., Battaglia, M.J., 2022. Assessing the broadscale effects of wildfire under extreme drought

- conditions to boreal peatlands. *Frontiers in Forests and Global Change* 5, 965605.
- Bowman, D.M., Kolden, C.A., Abatzoglou, J.T., Johnston, F.H., van der Werf, G.R., Flannigan, M., 2020. Vegetation fires in the anthropocene. *Nature Reviews Earth & Environment* 1, 500–515.
- Bradshaw, C.J., Warkentin, I.G., 2015. Global estimates of boreal forest carbon stocks and flux. *Global and Planetary Change* 128, 24–30.
- Buch, J., Williams, A.P., Juang, C.S., Hansen, W.D., Gentine, P., 2023. Smlfire1.0: a stochastic machine learning (sml) model for wildfire activity in the western united states. *Geoscientific Model Development* 16, 3407–3433.
- Byrne, B., Liu, J., Bowman, K.W., Pascolini-Campbell, M., Chatterjee, A., Pandey, S., Miyazaki, K., van der Werf, G.R., Wunch, D., Wennberg, P.O., et al., 2024. Carbon emissions from the 2023 canadian wildfires. *Nature* 633, 835–839.
- Calef, M., McGuire, A., Chapin III, F., 2008. Human influences on wildfire in alaska from 1988 through 2005: an analysis of the spatial patterns of human impacts. *Earth Interactions* 12, 1–17.
- Camps-Valls, G., Tuia, D., Zhu, X.X., Reichstein, M., 2021. Deep learning for the Earth Sciences: A comprehensive approach to remote sensing, climate science and geosciences. John Wiley & Sons.
- Chen, C., Li, O., Tao, D., Barnett, A., Rudin, C., Su, J.K., 2019. This looks like that: deep learning for interpretable image recognition. *Advances in neural information processing systems* 32.
- Chen, T., Kornblith, S., Norouzi, M., Hinton, G., 2020. A simple framework for contrastive learning of visual representations, in: International conference on machine learning, PmLR. pp. 1597–1607.
- Chen, Y., Romps, D.M., Seeley, J.T., Veraverbeke, S., Riley, W.J., Mekonnen, Z.A., Randerson, J.T., 2021. Future increases in arctic lightning and fire risk for permafrost carbon. *Nature Climate Change* 11, 404–410.

- Chowdhury, E.H., Hassan, Q.K., 2015. Operational perspective of remote sensing-based forest fire danger forecasting systems. *ISPRS Journal of Photogrammetry and Remote Sensing* 104, 224–236.
- Cong, Y., Khanna, S., Meng, C., Liu, P., Rozi, E., He, Y., Burke, M., Lobell, D., Ermon, S., 2022. Satmae: Pre-training transformers for temporal and multi-spectral satellite imagery. *Advances in Neural Information Processing Systems* 35, 197–211.
- Coughlan, R., Di Giuseppe, F., Vitolo, C., Barnard, C., Lopez, P., Drusch, M., 2021. Using machine learning to predict fire-ignition occurrences from lightning forecasts. *Meteorological applications* 28, e1973.
- Cunningham, C.X., Williamson, G.J., Bowman, D.M., 2024. Increasing frequency and intensity of the most extreme wildfires on earth. *Nature ecology & evolution* 8, 1420–1425.
- De Jong, M.C., Wooster, M.J., Kitchen, K., Manley, C., Gazzard, R., McCall, F.F., 2016. Calibration and evaluation of the canadian forest fire weather index (fwi) system for improved wildland fire danger rating in the united kingdom. *Natural Hazards and Earth System Sciences* 16, 1217–1237.
- Dosovitskiy, A., 2020. An image is worth 16x16 words: Transformers for image recognition at scale. *arXiv preprint arXiv:2010.11929* .
- Ekim, B., Schmitt, M., 2023. Explaining multimodal data fusion: Occlusion analysis for wilderness mapping, in: *IGARSS 2023-2023 IEEE International Geoscience and Remote Sensing Symposium*, IEEE. pp. 962–965.
- Fasihi, M., Sodini, M., Falcon, A., Degano, F., Sivilotti, P., Serra, G., 2025. Boosting grapevine phenological stages prediction based on climatic data by pseudo-labeling approach. *Artificial Intelligence in Agriculture* .
- Fernández-Llamazares, Á., Lepofsky, D., Lertzman, K., Armstrong, C.G., Brondizio, E.S., Gavin, M.C., Lyver, P.O., Nicholas, G.P., Pascua, P., Reo, N.J., et al., 2021. Scientists’ warning to humanity on threats to indigenous and local knowledge systems. *Journal of Ethnobiology* 41, 144–169.
- Fraser, A., Dastoor, A., Ryjkov, A., 2018. How important is biomass burning in canada to mercury contamination? *Atmospheric Chemistry and Physics* 18, 7263–7286.

- Gee, A.H., Garcia-Olano, D., Ghosh, J., Paydarfar, D., 2019. Explaining deep classification of time-series data with learned prototypes, in: CEUR workshop proceedings, p. 15.
- Geng, Y.a., Li, Q., Lin, T., Jiang, L., Xu, L., Zheng, D., Yao, W., Lyu, W., Zhang, Y., 2019. Lightnet: A dual spatiotemporal encoder network model for lightning prediction, in: Proceedings of the 25th ACM SIGKDD international conference on knowledge discovery & data mining, pp. 2439–2447.
- Ghosal, G.R., Abbasi-Asl, R., 2021. Multi-modal prototype learning for interpretable multivariable time series classification. arXiv preprint arXiv:2106.09636 .
- Gorishniy, Y., Rubachev, I., Babenko, A., 2022. On embeddings for numerical features in tabular deep learning. *Advances in Neural Information Processing Systems* 35, 24991–25004.
- Hall, R., Skakun, R., Metsaranta, J., Landry, R., Fraser, R., Raymond, D., Gartrell, M., Decker, V., Little, J., 2020. Generating annual estimates of forest fire disturbance in canada: the national burned area composite. *International journal of wildland fire* 29, 878–891.
- He, K., Chen, X., Xie, S., Li, Y., Dollár, P., Girshick, R., 2022. Masked autoencoders are scalable vision learners, in: Proceedings of the IEEE/CVF conference on computer vision and pattern recognition, pp. 16000–16009.
- He, K., Fan, H., Wu, Y., Xie, S., Girshick, R., 2020. Momentum contrast for unsupervised visual representation learning, in: Proceedings of the IEEE/CVF conference on computer vision and pattern recognition, pp. 9729–9738.
- He, K., Zhang, X., Ren, S., Sun, J., 2016. Deep residual learning for image recognition, in: Proceedings of the IEEE conference on computer vision and pattern recognition, pp. 770–778.
- Hoang, T.N., Truong, S., Schmidt, C., 2022. Wildfire forecasting with satellite images and deep generative model. arXiv preprint arXiv:2208.09411 .

- Hong, D., Zhang, B., Li, X., Li, Y., Li, C., Yao, J., Yokoya, N., Li, H., Ghamisi, P., Jia, X., et al., 2024. Spectralgpt: Spectral remote sensing foundation model. *IEEE Transactions on Pattern Analysis and Machine Intelligence* .
- Hu, E.J., Shen, Y., Wallis, P., Allen-Zhu, Z., Li, Y., Wang, S., Wang, L., Chen, W., et al., 2022. Lora: Low-rank adaptation of large language models. *ICLR* 1, 3.
- Huot, F., Hu, R.L., Goyal, N., Sankar, T., Ihme, M., Chen, Y.F., 2022. Next day wildfire spread: A machine learning dataset to predict wildfire spreading from remote-sensing data. *IEEE Transactions on Geoscience and Remote Sensing* 60, 1–13.
- Huot, F., Hu, R.L., Ihme, M., Wang, Q., Burge, J., Lu, T., Hickey, J., Chen, Y.F., Anderson, J., 2020. Deep learning models for predicting wildfires from historical remote-sensing data. *arXiv preprint arXiv:2010.07445* .
- Jain, P., Barber, Q.E., Taylor, S.W., Whitman, E., Castellanos Acuna, D., Boulanger, Y., Chavardès, R.D., Chen, J., Englefield, P., Flannigan, M., et al., 2024. Drivers and impacts of the record-breaking 2023 wildfire season in canada. *Nature Communications* 15, 6764.
- Jain, P., Coogan, S.C., Subramanian, S.G., Crowley, M., Taylor, S., Flannigan, M.D., 2020. A review of machine learning applications in wildfire science and management. *Environmental Reviews* 28, 478–505.
- Jakubik, J., Roy, S., Phillips, C., Fraccaro, P., Godwin, D., Zadrozny, B., Szwarcman, D., Gomes, C., Nyirjesy, G., Edwards, B., et al., 2023. Foundation models for generalist geospatial artificial intelligence. *arXiv preprint arXiv:2310.18660* .
- Jones, M.W., Kelley, D.I., Burton, C.A., Di Giuseppe, F., Barbosa, M.L.F., Brambleby, E., Hartley, A.J., Lombardi, A., Mataveli, G., McNorton, J.R., et al., 2024. State of wildfires 2023–2024. *Earth System Science Data* 16, 3601–3685.
- Keenan, T., Williams, C., 2018. The terrestrial carbon sink. *Annual Review of Environment and Resources* 43, 219–243.

- Klemmer, K., Rolf, E., Robinson, C., Mackey, L., Rußwurm, M., 2023. Sat-clip: Global, general-purpose location embeddings with satellite imagery. arXiv preprint arXiv:2311.17179 .
- Koh, P.W., Nguyen, T., Tang, Y.S., Mussmann, S., Pierson, E., Kim, B., Liang, P., 2020. Concept bottleneck models, in: International conference on machine learning, PMLR. pp. 5338–5348.
- Kohlenberg, A.J., Turetsky, M.R., Thompson, D.K., Branfireun, B.A., Mitchell, C.P., 2018. Controls on boreal peat combustion and resulting emissions of carbon and mercury. *Environmental Research Letters* 13, 035005.
- Kondylatos, S., Prapas, I., Ronco, M., Papoutsis, I., Camps-Valls, G., Piles, M., Fernández-Torres, M.Á., Carvalhais, N., 2022. Wildfire danger prediction and understanding with deep learning. *Geophysical Research Letters* 49, e2022GL099368.
- Krawchuk, M.A., Moritz, M.A., Parisien, M.A., Van Dorn, J., Hayhoe, K., 2009. Global pyrogeography: the current and future distribution of wildfire. *PloS one* 4, e5102.
- Li, L., Zhou, T., Wang, W., Li, J., Yang, Y., 2022. Deep hierarchical semantic segmentation, in: Proceedings of the IEEE/CVF Conference on Computer Vision and Pattern Recognition, pp. 1246–1257.
- Li, X.Y., Jin, H.J., Wang, H.W., Marchenko, S.S., Shan, W., Luo, D.L., He, R.X., Spektor, V., Huang, Y.D., Li, X.Y., et al., 2021. Influences of forest fires on the permafrost environment: A review. *Advances in Climate Change Research* 12, 48–65.
- Lindenmayer, D.B., Franklin, J.F., 2013. *Conserving forest biodiversity: a comprehensive multiscaled approach*. Island press.
- Liu, Z., Deng, Z., Davis, S.J., Ciais, P., 2024. Global carbon emissions in 2023. *Nature Reviews Earth & Environment* 5, 253–254.
- Lundberg, S.M., Lee, S.I., 2017. A unified approach to interpreting model predictions. *Advances in neural information processing systems* 30.

- Martell, D.L., Bevilacqua, E., Stocks, B.J., 1989. Modelling seasonal variation in daily people-caused forest fire occurrence. *Canadian Journal of Forest Research* 19, 1555–1563.
- Martell, D.L., Otukol, S., Stocks, B.J., 1987. A logistic model for predicting daily people-caused forest fire occurrence in ontario. *Canadian Journal of Forest Research* 17, 394–401.
- McCarty, J.L., Aalto, J., Paunu, V.V., Arnold, S.R., Eckhardt, S., Klimont, Z., Fain, J.J., Evangelidou, N., Venäläinen, A., Tchebakova, N.M., et al., 2021. Reviews & syntheses: arctic fire regimes and emissions in the 21st century. *Biogeosciences Discussions* 2021, 1–59.
- Milanović, S., Marković, N., Pamučar, D., Gigović, L., Kostić, P., Milanović, S.D., 2020. Forest fire probability mapping in eastern serbia: Logistic regression versus random forest method. *Forests* 12, 5.
- Natekar, S., Patil, S., Nair, A., Roychowdhury, S., 2021. Forest fire prediction using lstm, in: *2021 2nd International Conference for Emerging Technology (INCET)*, IEEE. pp. 1–5.
- Oquab, M., Darcet, T., Moutakanni, T., Vo, H., Szafraniec, M., Khalidov, V., Fernandez, P., Haziza, D., Massa, F., El-Nouby, A., et al., 2023. Dino2: Learning robust visual features without supervision. *arXiv preprint arXiv:2304.07193* .
- Pan, Y., Birdsey, R.A., Phillips, O.L., Houghton, R.A., Fang, J., Kauppi, P.E., Keith, H., Kurz, W.A., Ito, A., Lewis, S.L., et al., 2024. The enduring world forest carbon sink. *Nature* 631, 563–569.
- Pelletier, N., Millard, K., Darling, S., 2023. Wildfire likelihood in canadian treed peatlands based on remote-sensing time-series of surface conditions. *Remote Sensing of Environment* 296, 113747.
- Pérez-Invernón, F.J., Gordillo-Vázquez, F.J., Huntrieser, H., Jöckel, P., 2023. Variation of lightning-ignited wildfire patterns under climate change. *Nature communications* 14, 739.
- Porta, H., Dalsasso, E., Marcos, D., Tuia, D., 2025a. Multi-scale grouped prototypes for interpretable semantic segmentation, in: *2025 IEEE/CVF*

- Winter Conference on Applications of Computer Vision (WACV), IEEE. pp. 2869–2880.
- Porta, H., Kamoun, I., Tuia, D., 2025b. Interpretable by-design wildfire forecasting via prototypes. Technical Report. Copernicus Meetings.
- Prapas, I., Ahuja, A., Kondylatos, S., Karasante, I., Panagiotou, E., Alonso, L., Davalas, C., Michail, D., Carvalhais, N., Papoutsis, I., 2022. Deep learning for global wildfire forecasting. arXiv preprint arXiv:2211.00534 .
- Prapas, I., Bountos, N.I., Kondylatos, S., Michail, D., Camps-Valls, G., Papoutsis, I., 2023. Televit: Teleconnection-driven transformers improve sub-seasonal to seasonal wildfire forecasting, in: Proceedings of the IEEE/CVF International Conference on Computer Vision, pp. 3754–3759.
- Prapas, I., Kondylatos, S., Papoutsis, I., Camps-Valls, G., Ronco, M., Fernández-Torres, M.Á., Guillem, M.P., Carvalhais, N., 2021. Deep learning methods for daily wildfire danger forecasting. arXiv preprint arXiv:2111.02736 .
- Rashkovetsky, D., Mauracher, F., Langer, M., Schmitt, M., 2021. Wildfire detection from multisensor satellite imagery using deep semantic segmentation. *IEEE Journal of Selected Topics in Applied Earth Observations and Remote Sensing* 14, 7001–7016.
- Reichstein, M., Camps-Valls, G., Stevens, B., Jung, M., Denzler, J., Carvalhais, N., Prabhat, F., 2019. Deep learning and process understanding for data-driven earth system science. *Nature* 566, 195–204.
- Rodrigues, E., Watson, C.D., Nyirjesy, G., Nathaniel, J., Zadrozny, B., 2022. Firo: A deep-neural network for wildfire forecast with interpretable hidden states. *Climate Change AI* 2.
- Růžička, V., Vaughan, A., De Martini, D., Fulton, J., Salvatelli, V., Bridges, C., Mateo-Garcia, G., Zantedeschi, V., 2022. Ravæn: Unsupervised change detection of extreme events using ml on-board satellites. *Scientific Reports* 12, 16939.
- Sacha, M., Rymarczyk, D., Struski, Ł., Tabor, J., Zieliński, B., 2023. Protoseg: Interpretable semantic segmentation with prototypical parts, in:

- Proceedings of the IEEE/CVF Winter Conference on Applications of Computer Vision, pp. 1481–1492.
- Schmale, J., Zieger, P., Ekman, A.M., 2021. Aerosols in current and future arctic climate. *Nature Climate Change* 11, 95–105.
- Selvaraju, R.R., Cogswell, M., Das, A., Vedantam, R., Parikh, D., Batra, D., 2017. Grad-cam: Visual explanations from deep networks via gradient-based localization, in: Proceedings of the IEEE international conference on computer vision, pp. 618–626.
- Steinfeld, D., Peter, A., Martius, O., Brönnimann, S., 2022. Assessing the performance of various fire weather indices for wildfire occurrence in northern switzerland. *EGUsphere* 2022, 1–23.
- Sundararajan, M., Taly, A., Yan, Q., 2017. Axiomatic attribution for deep networks, in: International conference on machine learning, PMLR. pp. 3319–3328.
- Turbé, H., Bjelogrić, M., Lovis, C., Mengaldo, G., 2023. Evaluation of post-hoc interpretability methods in time-series classification. *Nature Machine Intelligence* 5, 250–260.
- Tyukavina, A., Potapov, P., Hansen, M.C., Pickens, A.H., Stehman, S.V., Turubanova, S., Parker, D., Zalles, V., Lima, A., Kommareddy, I., et al., 2022. Global trends of forest loss due to fire from 2001 to 2019. *Frontiers in Remote Sensing* 3, 825190.
- Vivanco Cepeda, V., Nayak, G.K., Shah, M., 2023. Geoclip: Clip-inspired alignment between locations and images for effective worldwide geolocalization. *Advances in Neural Information Processing Systems* 36, 8690–8701.
- Waddington, J., Thompson, D., Wotton, M., Quinton, W., Flannigan, M., Bencoter, B., Baisley, S., Turetsky, M., 2012. Examining the utility of the canadian forest fire weather index system in boreal peatlands. *Canadian Journal of Forest Research* 42, 47–58.
- Wang, Y., Rudner, T.G., Wilson, A.G., 2023. Visual explanations of image-text representations via multi-modal information bottleneck attribution. *Advances in Neural Information Processing Systems* 36, 16009–16027.

- Weilhammer, V., Schmid, J., Mittermeier, I., Schreiber, F., Jiang, L., Pastuhovic, V., Herr, C., Heinze, S., 2021. Extreme weather events in europe and their health consequences—a systematic review. *International Journal of Hygiene and Environmental Health* 233, 113688.
- Wotton, B.M., 2009. Interpreting and using outputs from the canadian forest fire danger rating system in research applications. *Environmental and ecological statistics* 16, 107–131.
- Yang, S., Lupascu, M., Meel, K.S., 2021. Predicting forest fire using remote sensing data and machine learning, in: *Proceedings of the AAAI conference on artificial intelligence*, pp. 14983–14990.
- Zbinden, R., Van Tiel, N., Kellenberger, B., Hughes, L., Tuia, D., 2024. On the selection and effectiveness of pseudo-absences for species distribution modeling with deep learning. *Ecological Informatics* 81, 102623.
- Zhang, B., Wang, H., Alabri, A., Bot, K., McCall, C., Hamilton, D., Růžička, V., 2022. Unsupervised wildfire change detection based on contrastive learning. *arXiv preprint arXiv:2211.14654* .
- Zhang, G., Wang, M., Liu, K., 2021. Deep neural networks for global wildfire susceptibility modelling. *Ecological Indicators* 127, 107735.
- Zhang, Y., Yang, Q., 2021. A survey on multi-task learning. *IEEE transactions on knowledge and data engineering* 34, 5586–5609.
- Zhao, J., Yue, C., Wang, J., Hantson, S., Wang, X., He, B., Li, G., Wang, L., Zhao, H., Luysaert, S., 2024. Forest fire size amplifies postfire land surface warming. *Nature* 633, 828–834.